Urban Climate 62 (2025) 102564

Contents lists available at ScienceDirect

Urban Climate

journal homepage: www.elsevier.com/locate/uclim

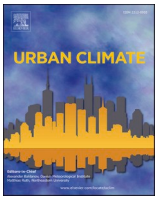

Deep learning enables city-wide climate projections of street-level heat stress

Ferdinand Briegel [a,b,*], Simon Schrodi [c], Markus Sulzer [b], Thomas Brox [c], Joaquim G. Pinto [a], Andreas Christen [b]

[a] Institute of Meteorology and Climate Research Troposphere Research (IMKTRO), Karlsruhe Institute of Technology (KIT), Karlsruhe, Germany
[b] Chair of Environmental Meteorology, Faculty of Environment and Natural Resources, University of Freiburg, Freiburg im Breisgau, Germany
[c] Department of Computer Science, University of Freiburg, Freiburg im Breisgau, Germany

ARTICLE INFO

Keywords:
Thermal comfort
Urban climate
Deep learning
Building resolved
Downscaling climate projections

ABSTRACT

Urban areas are increasingly vulnerable to the impacts of climate change, especially heatwaves, due to their distinct characteristics. However, the influence of urban form and land cover on future outdoor thermal comfort remains inadequately quantified in climate models. This study addresses this issue by introducing the Unified Human Thermal Comfort Neural Network (UHTC-NN), a novel deep learning framework that efficiently and accurately maps pedestrian-level urban heat stress at a building-resolved scale of 1 m across entire cities. Using the city of Freiburg, Germany, as a case study, the model uses extensive spatial data to generate detailed Universal Thermal Climate Index (UTCI) maps by downscaling CMIP5 climate ensembles for the period 2070–2099. The model results show significant increases in heat stress hours under future climate scenarios (RCP4.5 and RCP8.5), with climate signals emerging as the dominant effect. Our model reveals that future heat stress hours will exhibit significant spatial variability, with contrasting day-night dynamics. While overall heat stress hours (UTCI $\geq$ 26 °C) increase more uniformly during the day, nighttime heat stress hours and daytime extremes (UTCI $\geq$ 38 °C) increase more heterogeneously. These patterns are significantly influenced by shading and radiation trapping at the meter scale, and by building density and land cover at the hectometer scale. This work highlights the need for high-resolution models to accurately map urban heat exposure and inform adaptive urban planning. By facilitating comprehensive analyses, the model supports targeted interventions to mitigate urban heat, providing a local-specific tool for urban planning in a warming world.

1. Introduction

Urban areas stand at the forefront of climate change impacts, as they are more vulnerable to weather and climate extreme events such as heatwaves, flooding, or low air quality (Oke et al., 2017; Unger et al., 2020). With more than 55 % of the world's population living in cities (United Nations et al., 2019), this poses a significant risk to human well-being, particularly in terms of heat stress (Mora et al., 2017), but also regard to economic losses, increased risk of power outages (Stone et al., 2021), and increased mortality due to

* Corresponding author at: Institute of Meteorology and Climate Research Troposphere Research (IMKTRO), Karlsruhe Institute of Technology (KIT), Karlsruhe, Germany.
E-mail address: ferdinand.briegel@kit.edu (F. Briegel).

https://doi.org/10.1016/j.uclim.2025.102564
Received 21 February 2025; Received in revised form 29 May 2025; Accepted 30 July 2025
Available online 7 August 2025

extreme events (Cissé et al., 2022; Dodman et al., 2022).

The frequency and intensity of regional heatwaves has already increased worldwide in recent decades (Barriopedro et al., 2011; Perkins-Kirkpatrick and Lewis, 2020). Even a 0.5 K increase in global warming will significantly increase both the intensity and frequency of extreme heat events (Seneviratne et al., 2021). Furthermore, the global urban population is estimated to increase from 55 % to 68 % by 2050 (United Nations et al., 2019), highlighting the need to address the vulnerability of urban areas to extreme heat events by adapting to and mitigating the impacts of urban heat (Wang et al., 2021; Barriopedro et al., 2023).

The characteristics of urban areas differ in form and function from those of rural areas, causing very specific urban canopy climates, often with large intra-urban and microscale variability (Fenner et al., 2017; Masson et al., 2020; Yang et al., 2024). Generally, cities have a higher proportion of paved areas, enlarged three-dimensional surface areas for heat storage, complex shadow patterns, and a lower proportion of vegetation and permeable surface (Oke et al., 2017). This results in an altered energy and water balance compared to rural areas, leading to the Urban Heat Island effect (UHI; Oke, 1982). There are four types of UHI: sub-surface, surface, canopy and boundary layer. The canopy and surface UHI are particularly relevant for thermal comfort assessments as the UHI effect can result in increased and differently timed heat stress for pedestrians, especially in summer and during heatwaves (Best and Grimmond, 2015; Ward et al., 2016a, 2016b; Lamberti et al., 2025). Therefore, the built environments of urban areas strongly affect human thermal comfort, particularly due to increased heat loads at night. Human thermal comfort, and therefore heat stress, is influenced not only by air temperature (T_a; °C), but also by relative humidity (RH; %), three-dimensional radiation load (expressed as mean radiant temperature - T_{mrt}; °C), wind velocity (U; m s^{-1}) (Parsons, 2002), and physiological factors such as metabolic rate or clothing insulation (Epstein and Moran, 2006). To summarize these effects into a single equivalent (perceived) temperature, several thermal indices have been developed (de Freitas and Grigorieva, 2017). In this study, the Universal Thermal Climate Index (UTCI; °C) (Błażejczyk et al., 2013) is used, as it is one of the indices that has been the focus of past and future research on outdoor thermal comfort from micro- (Nice et al., 2022; Weeding et al., 2024) over meso- (Nam et al., 2024) to global scale (Di Napoli et al., 2021). UTCI provides a standardized measure of thermal comfort based on the physiological responses of a reference individual (Fiala model - Fiala et al., 2001) walking outdoors under reference conditions of 50 % RH, U of 0.5 m s^{-1} at 10 m, and T_{mrt} equal to T_a.

Modelling the impact of urban form and function on outdoor thermal comfort during extreme weather events such as heatwaves has received considerable attention in recent years (Krayenhoff et al., 2021). Most models are process-based, meaning they resolve physical processes such as radiative transfer (Lindberg et al., 2008, 2018), heat storage (Järvi et al., 2011; Ward et al., 2016a), energy partitioning (Järvi et al., 2011; Lindberg et al., 2018), and airflow (Giometto et al., 2016, 2017; Wehrle et al., 2024) at different urban scales, which is computationally expensive and time consuming (Briegel et al., 2023). For this reason, previous research assessing future outdoor thermal comfort in cities has been limited to case studies of individual neighborhoods or generic locations (Aminipouri et al., 2019; Wallenberg et al., 2023; Weeding et al., 2024), coarse spatial resolution (Krayenhoff et al., 2018; Zhao et al., 2021; Georgescu et al., 2023; Hundhausen et al., 2023), short time periods or single days, and often with a focus solely on T_a (Paranunzio et al., 2021) or T_{mrt} (Aminipouri et al., 2019). This means that research focusing on the temporal dimension, by modelling thermal comfort over long time periods, is limited by spatial resolution. On the other hand, studies that focus on high spatial resolution and/or larger model domains are limited to short exemplary time periods (Nice et al., 2022). Although a combination of long-term modelling of a generic point and spatial modelling of extreme events has been carried out (Lindberg et al., 2016; Thorsson et al., 2017), a combination of high temporal and spatial resolution on large model domains, resolving all buildings of entire cities over decades, has not been possible due to disproportionate computational effort.

In recent years, machine and deep learning approaches that emulate process-based models in different fields of urban climate sciences have gained more and more attention as a potential solution to the temporal and spatial shortcomings of process-based urban climate models (Luo and Chen, 2025). For example, image-to-image deep learning approaches, such as U-Net (Ronneberger et al., 2015), have become popular due to their ability to enable spatial predictions. Lu et al. (2025) and Briegel et al. (2023) both used a U-Net to emulate LES/SOLWEIG for U and T_{mrt} predictions, respectively. Delgado-Enales et al. (2025) applied a U-Net to model spatial fields of T_a in Bilbao, Spain. The work by Briegel et al. (2024) proposed a combined model of different machine and deep learning based sub-models to model T_a, U, RH, and T_{mrt} individually in the first instance, and outdoor thermal comfort (UTCI) in the second instance. However, this approach involves dividing the complex interactions influencing outdoor thermal comfort into sub-models for each meteorological variable. While this modular structure is functional since the relevant variables can be assessed independently, it introduces inefficiencies. Although previous studies have demonstrated the strong predictive capabilities of U-Nets for individual variables (Delgado-Enales et al., 2025; Lu et al., 2025), there is currently no universal deep learning-based model capable of directly predicting spatially continuous UTCI fields.

In this study, we present the Unified Human Thermal Comfort Neural Network (UHTC-NN), a streamlined deep learning model based on the previous model (Briegel et al., 2024) that directly predicts spatial fields of UTCI based on geospatial inputs and temporally varying meteorological forcings. This streamlined model, using a single unified neural network, is significantly faster and more efficient than its predecessor, achieving up to 10^6 times the speed of traditional numerical models. The rapid prediction of two-dimensional UTCI fields in urban environments allows high-resolution, city-wide, long-term climate impact assessments across multiple scales with reasonable computational effort (hours to days), providing a systematic and quantitative analysis of urban heat stress that has not been possible before. After validation and, if necessary, further training for specific urban settings, the model can be adapted and applied to any city.

We demonstrate the model's advantages and the impact of climate change at pedestrian level using Freiburg, a mid-sized city in Southwest Germany, as a showcase. Here, UHTC-NN is used to provide city-wide high-resolution (1 m) pedestrian level UTCI maps. We compare an ensemble of CMIP5 global-to-regional climate model chains for the years 2070–2099 with the historical climate from downscaled reanalysis data (ERA5-Land) for the years 1990–2019 (historical reference period). This comparison includes three

Representative Concentration Pathways (RCP2.6, RCP4.5, and RCP8.5). A detailed mapping of heat stress hours to land cover classes at different spatial scales is performed. The UHTC-NN allows us to investigate whether future heat extremes will increase uniformly across the city or exhibit spatial patterns of differential warming. Furthermore, the UHTC-NN facilitates the analysis of how urban heat extremes are related to urban form and land cover. This information is crucial for identifying effective heat adaptation measures, such as optimizing building density and enhancing green and blue infrastructure.

2. Methods

The following section gives an overview of the study area and how temporal and spatial data are derived from different sources as well as validation data. In addition, the pre-processing process of temporal and spatial data to receive the model predictors is described. Furthermore, the entire model development process with validation and prediction is given.

2.1. Study area

The study area covers the urbanized area of Freiburg im Breisgau, Germany, a mid-latitude city in Central Europe. The mid-sized city is located in Southwest Germany (48.0°N, 7.8°E) in the Upper Rhine Valley and at the western slope of the Black Forest Mountain range. Freiburg has a warm-temperate climate with long-term averages (1990–2020) of 11.0 °C for annual T_a (20.1 °C in July), 886.5 mm for annual precipitation, and up to 19 days with maximum $T_a > 30$ °C per year (DWD Climate Data Center (CDC), 2025). However, the average annual T_a of the last 10 years (2015–2024) was almost 1 K warmer than the long-term average of 11.9 °C. In addition, Hundhausen et al. (2023) showed that the Rhine Valley is one of the most exposed areas to heat stress in Germany and is predicted to experience a disproportionate increase in the future.

The training domain covers the urbanized area of Freiburg and has an extent of 10 km × 7 km and the model domain for downscaling climate model data has an extent of 5.0 km × 2.5 km (Fig. 1). The training domain provides detailed data from 40+ weather stations in an street-level sensor network, which helps to validate the model's accuracy (Zeeman et al., 2024). Possible future changes in land use, urban development scenarios or changes in ecosystem functions are not considered as this would require further assumptions. However, this does not preclude such applications; for example, the UHTC-NN can be used to optimize buildings (Fünfgeld et al., 2025) or vegetation (Schrodi et al., 2023) for thermal comfort.

2.2. Climate change scenarios and reanalysis data

Reanalysis data for the years 1990–2019 are used as reference data to compare heat stress in future urban climates with the current urban climate assuming urban form stays constant. For this purpose, ERA5-Land data are used as provided by the Copernicus Climate

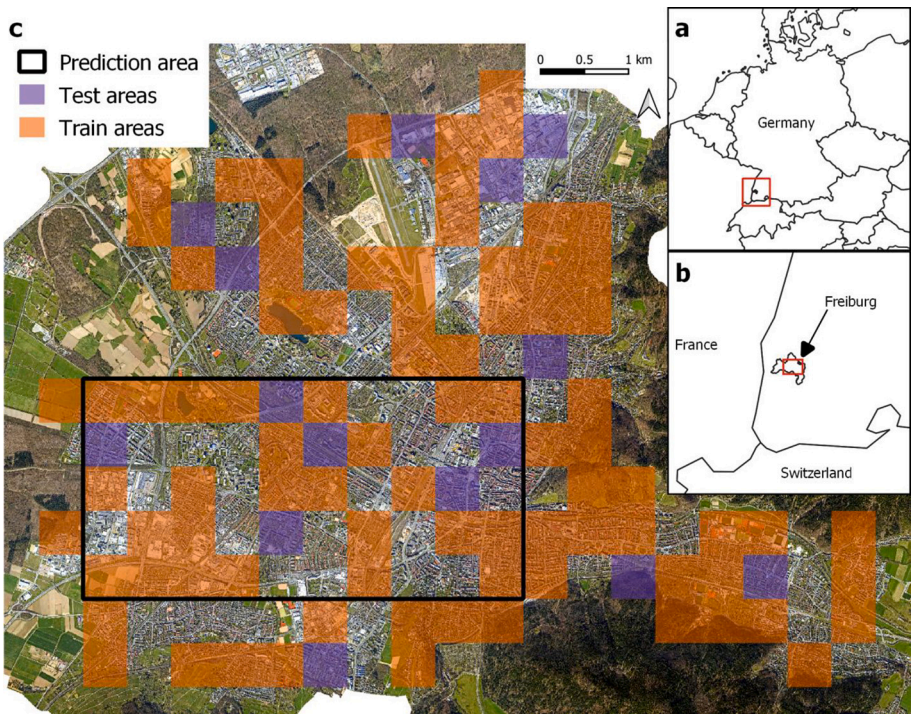

Fig. 1. Study area with train, test, and prediction areas (**c**) and the location of Freiburg in Germany (**a** and **b**).

Data Store (Muñoz Sabater, 2019, 2021). ERA5-Land data have a spatial resolution of ~9 km, allowing for detailed analysis of land surface conditions. ERA5-Land data are aggregated to 3 h values to ensure comparability, as the climate model data have a 3 h temporal resolution.

CMIP5 climate model data from five global-to-regional climate model chains (GCM-RCM) with a spatial resolution of 0.11° (~12.5 km) are used as forcing data for thermal comfort predictions, consisting of three different global models and two different regional models (Table 1). For each, three different representative concentration pathways are considered, namely RCP2.6, RCP4.5, and RCP8.5 for the period 2070–2099. The peak of anthropogenic radiation forcing in RCP2.6 is assumed to occur in the mid-21st century, resulting in a forcing of 2.6 W m^{-2} in 2100 (van Vuuren et al., 2011). RCP4.5 is a scenario with a stabilization of the radiative forcing at 4.5 W m^{-2} by the end of the century, while RCP8.5 is a scenario with very high greenhouse gas emissions, leading to a radiative forcing of 8.5 W m^{-2} in 2100 (van Vuuren et al., 2011). The ensemble of simulations with different global and regional climate model chains is considered to provide a more comprehensive view of climate change projections in terms of regional heat extremes and uncertainty estimation. These simulations are part of the EURO-CORDEX dataset (https://www.euro-cordex.net). Only model chains for which all three RCPs were available in the Copernicus Climate Data Store (Copernicus Climate Change Service and Climate Data Store, 2019) could be considered. The climate model data and ERA5-Land data were extracted from the specific grid cell containing the Freiburg model domain (5.0 km × 2.5 km).

The climate model data are bias corrected in two steps. For this purpose, the R package "Multivariate Bias Correction of Climate Model Outputs" is used (Cannon Alex, 2023). In the first step univariate quantile delta mapping (QDM) (Cannon, 2016; Fauzi et al., 2020; Qian and Chang, 2021) is applied. Therefore, quantiles of the ERA5-Land data and historical climate model data are mapped for the period of 1970–1999 and then applied to the climate model data of 2070–2099. For a more detailed description of the QDM method applied to the climate model data see Sulzer and Christen (2024). In the second step, the Multivariate Bias Correction in N dimensions (MBCn) as introduced by Cannon (2018) is applied, which is an extension of the univariate QDM method to multiple dimensions. Multivariate bias correction is applied to account for the interactions of the meteorological data that need to be considered for the UTCI calculation. To account for seasonality and the diurnal cycle, data are grouped by month and hour of the day prior to both bias correction steps. Figure A1 (Appendix A) shows detailed results of the bias correction process.

2.3. Validation data

Data from a custom biometeorological sensor network (Zeeman et al., 2024; Feigel et al., 2025) are used for pointwise validation of the UHTC-NN. The sensor network consists of eight stations. The sensors measure T_a, RH, U, and black globe temperature (Feigel et al., 2025), which allows the calculation of T_{mrt} and hence UTCI (Błażejczyk et al., 2013). The stations are distributed across the entire city and its surroundings and represent different urban areas such as residential or industrial areas (Plein et al., 2024). Detailed information on the sensor network and its custom data logging and management platform can be found in Plein et al. (2024) and Zeeman et al. (2024). The biometeorological stations are instrumented with full weather sensors (ClimaVUE50, Campbell Scientific Inc., Logan, UT, USA) and black globe temperature sensors (model BLACKGLOBE-L, Campbell Scientific Inc., Logan, UT, USA) which are connected to a custom data logging platform (Feigel et al., 2025). The sensors are mounted at 3 m a.g.l. on streetlights or custom poles with south facing black globes to ensure full sun exposition (Feigel et al., 2025). The measuring interval is one minute.

2.4. Model development

The following sections describe the derivation of the spatial and temporal predictors and the response data (UTCI maps), the model development process, and the model evaluation process and predictions. The deep learning modelling is done using Python (Python Software Foundation) and PyTorch (Paszke et al., 2019). The UHTC-NN model requires geospatial input in the form of detailed urban building, form, and vegetation characteristics, and temporally varying input in the form of generic meteorological forcing for the entire domain.

2.4.1. Spatial and temporal predictors

The spatial predictors are related to urban form and function and are time independent. All spatial predictors are listed in Table 2. Since the UHTC-NN combines several sub-models of the proposed model by Briegel et al. (2024) into one, spatial predictors are added to the UHTC-NN in two different ways: spatially resolved and spatially aggregated (see Fig. 2). Spatially resolved data are provided to the U-Net encoder as images (matrices) with a resolution of 1 m and an extent of 500 m × 500 m, such as the Digital Surface Model

Table 1
Overview of the used CMIP5 EURO-CORDEX simulations. GCM: Global Climate Model; RGM: Regional Climate Model; RCP: Representative Concentration Pathway; rip: realization, initialization, and physics (driving ensemble member).

GCM	RCM	rip	RCP
ICHEC-EC-EARTH	KNMI-RACMO22E	r12i1p1	RCP2.6, RCP4.5, RCP8.5
ICHEC-EC-EARTH	SMHI-RCA4	r12i1p1	RCP2.6, RCP4.5, RCP8.5
MOHC-HadGEM2-ES	KNMI-RACMO22E	r1i1p1	RCP2.6, RCP4.5, RCP8.5
MOHC-HadGEM2-ES	SMHI-RCA4	r1i1p1	RCP2.6, RCP4.5, RCP8.5
MPI-M-MPI-ESM-LR	SMHI-RCA4	r1i1p1	RCP2.6, RCP4.5, RCP8.5

(DSM), Digital Elevation Model (DEM), or Land Cover Classes (LCC - Briegel and Christen, 2025). Land cover data is based on information from several sources (Briegel et al., 2023) and follows the UMEP definitions (Lindberg et al., 2018). According to these, pixels with values such as 'grass', 'paved', 'water', and 'bare soil' do not have a tree canopy above them. DSM and DEM are obtained from LiDAR data provided by the city of Freiburg, and have a vertical accuracy of ±0.15 m (City of Freiburg im Breisgau, 2021). To prevent edge effects, several adjustments are made to the spatial data during pre-processing. Spatial predictors, such as Sky View Factor maps, are calculated not only for 500 m × 500 m grid cells, but also within a 200 m buffer. Spatially aggregated data covers the same 500 m × 500 m grid extent as the spatially resolved data, but aggregated into a scalar value: e.g., mean building height, mean altitude, or fractions of land cover classes. The aggregated spatial data are added together with the temporal data to the abstract spatial representation of the U-Net (the 'bottleneck' between encoder and decoder). A detailed description of the derivation of the spatially resolved and aggregated data can be found in Briegel et al. (2023, 2024), and Briegel and Christen (2025).

The temporal predictors are climate change scenario and reanalysis atmospheric forcing data. The variables derived from climate change scenario and reanalysis data are T_a, RH, air pressure, wind speed and direction, incoming shortwave radiation (Kdown), and incoming longwave radiation (Ldown). ERA5-Land data is used as training data. Besides these variables, additional temporal variables are created. To account for seasonality and the diurnal cycle, sine functions are applied with maximum and minimum in summer/winter and day/night. In addition to the sine functions, solar elevation and declination angles are added to address the position of the sun to better map shadow patterns. The temporal data, together with the spatial aggregated data (in sum 25 predictors), are added to the abstract spatial representation of the U-Net.

2.4.2. Response data

The response data comprises UTCI maps generated from simulations using the HTC-NN model by Briegel et al. (2024), which was proposed to model UTCI with high spatial and temporal resolution for large model domains. Their model uses four different sub-models based on machine and deep learning to separately model T_a, RH, T_{mrt}, and U, respectively. Due to the different spatial variability of the input variables, T_a and RH are modelled at a spatial resolution of 500 m, while T_{mrt} and U are modelled at a finer resolution of 1 m. Consequently, UTCI is predicted over areas of 500 m × 500 m using input data at mixed resolutions: 500 m for T_a and RH and 1 m for T_{mrt} and U. The individual sub-models are described in detail in Briegel et al. (2024) for T_a, RH, and U; in Wehrle et al. (2024) for U; and in Briegel et al. (2023) for T_{mrt}. The outputs from these four sub-models are used in the final step to calculate the UTCI.

2.4.3. Model development

The development of the UHTC-NN requires three steps: (i) splitting predictors and response data into training and test data (sampling), (ii) finding the best U-Net architecture, and (iii) training and evaluating the final model.

The spatial training and test data consist of 100 areas with a size of 500 m × 500 m (Fig. 1). The temporal training and test data consist of 200 days with an hourly resolution. Of the 100 areas, 85 are used for training and 15 are retained for testing. Likewise, of the 200 days, 170 are devoted to training and the remaining 30 to testing. This means, the HTC-NN is used to simulate UTCI maps for 85 areas and 170 days (training) and 15 areas and 30 days (testing) with hourly resolution, resulting in a total of 357,600 UTCI maps with 346,800 maps used for training and 10,800 for testing. Temporal training data are randomly sampled within the period from 2020 to 2022, while data sampled after the summer of 2022 serve as test data. Some days are added manually to cover extreme weather situations: days with minimum and maximum daily average T_a and days with daily minimum and maximum T_a are added. This means that 196 days are randomly sampled, and 4 days are predefined. Spatial training and test areas are also randomly sampled. Similar to the temporal data, specific test areas are predefined manually as biometeorological measurements exist in some areas. In total, 92 areas are randomly sampled, and 8 areas are manually defined. The spatial and temporal predictors are split into training and test data in the same way as the UTCI response data.

The final architecture of the UHTC-NN is based on the U-Net architecture proposed by Ronneberger et al. (2015) and Dosovitskiy et al. (2015). A more detailed explanation of the U-Net and its functionality can also be found in Briegel et al. (2023). A schematic representation of the model is shown in Fig. 2. The resolved spatial input data (34, 512, 512) is reshaped by a 3 × 3 convolutional layer (32, 512, 512) before being transformed into an abstract representation by three 3 × 3 convolutional layers with a stride of two resulting in a shape of (256, 64, 64). The aggregated spatial and the temporal data (256, 1, 1) are added to this abstract representation. This is followed by upsampling, concatenation with the specific encoder layer (skip connections), and a 1 × 1 convolutional layer. This process is repeated three times before a 3 × 3 convolutional layer is applied in the last step to achieve the targeted spatial resolution (1, 512, 512). Except for the last convolutional layer, batch normalization and ReLU activation function are added after to the convolutional layers. The model is trained for 10 epochs. The remaining hyperparameters are listed in Table A2.

Table 2
Spatial predictors of the UHTC-NN can be either spatially resolved (1 m × 1 m) or aggregated (500 m × 500 m). DSM: Digital Surface Model; DEM: Digital Elevation Model; SVF: Sky View Factor; suffixes 'b' and 'v' account for buildings and vegetation, respectively.

Urban form and function	Spatially resolved	Spatially aggregated
Building structure	DEM, DSMb, SVFb	Mean building height, roughness length, zero place displacement length, frontal area index
Vegetation structure	DEM, DSMv, SVFv	Mean vegetation height, frontal area index
Land cover classes	Land cover class map	Land cover class fractions, mean altitude
Urban population	–	Population density

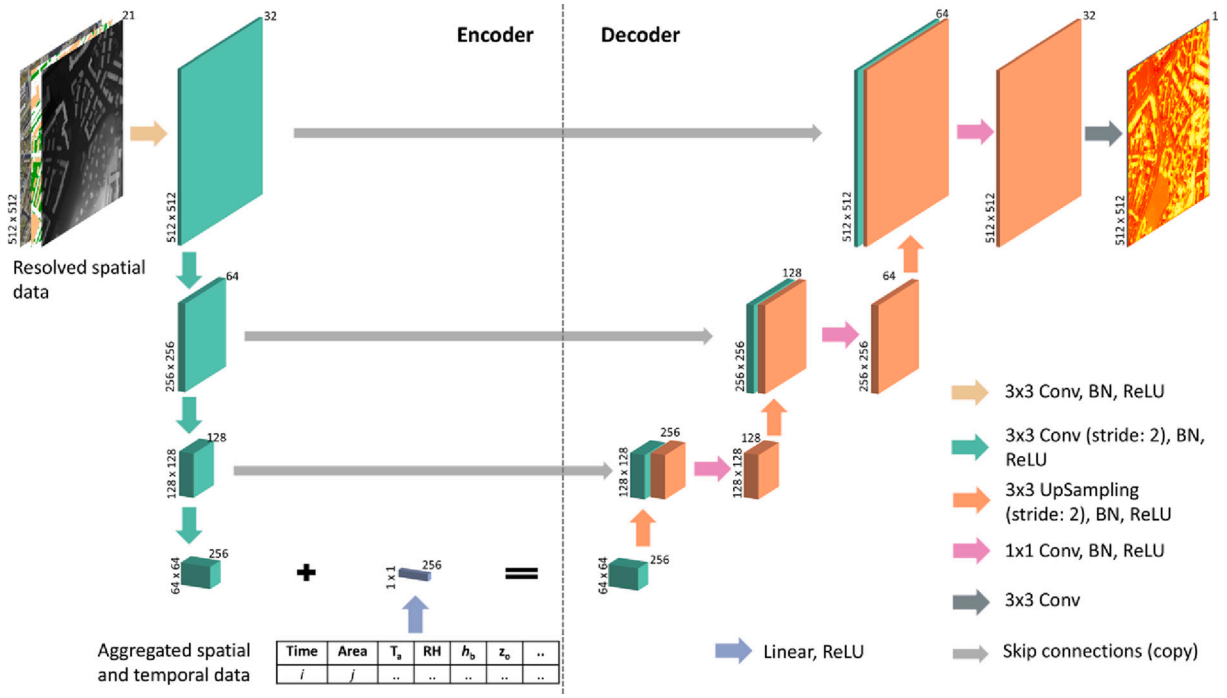

Fig. 2. Schematic representation of the U-Net (figure is based on Briegel et al., 2023).

The UHTC-NN is validated in two steps. The first step is a spatial validation against the model from Briegel et al. (2024). In a second step, both models are validated against measurements from the biometeorological sensor network. As evaluation measures Root Mean Square Error:

$$\boldsymbol{RMSE} = \sqrt{\frac{\mathbf{1}}{\boldsymbol{n}}\sum_{i=1}^{n}(\boldsymbol{y}_i - \widehat{\boldsymbol{y}}_i)^2} \tag{1}$$

and Mean Absolute Error:

$$\boldsymbol{MAE} = \frac{\mathbf{1}}{\boldsymbol{n}}\sum_{i=1}^{n}|\boldsymbol{y}_i - \widehat{\boldsymbol{y}}_i| \tag{2}$$

are used.

2.4.4. Model predictions

The UHTC-NN is used to model UTCI on a spatial resolution of 1 m and on temporal resolution of 3 h for the two periods from 1990 to 2019 and 2070–2099. For the 2070–2099 period, the UHTC-NN is forced with the RCP2.6, RCP4.5, and RCP8.5 scenarios using five climate models each. This results in 15 simulations for the 2070–2099 period.

The prediction area is a 5.0 km × 2.5 km subset of the city of Freiburg (see Fig. 1). In order to prevent edge effects (see Fig. B2), we ran two simulations of UTCI for the same model domain: one with the initial grid configuration and one with a shifted grid. This involved shifting the grid by 250 m in both the x and y directions to create overlapping grids and predictions. We then calculated a weighted mean based on the distance to the corresponding grid cell centres. This means roughly 140 million 500 m × 500 m UTCI maps and around 36 billion 1 m × 1 m UTCI point predictions are calculated. Since saving results of every individual timestep would exceed available storage capacity, only aggregated results are saved. The results are not stored as decimal numbers, but as sums of hours per pixel in each UTCI class. The bin size of the UTCI classes is 1 °C, e.g. [1.0 °C, 2.0 °C). In addition, a distinction is made between day and night and between months. This allows the calculation of the average hours per month and pixel above certain thresholds for both day and night.

2.5. Validation of the UHTC-NN

2.5.1. Validation

The validation of the UHTC-NN is done in two ways. A direct comparison with its parent model (Briegel et al., 2024) is performed, as well as point validations using RMSE for both models with measurements from a pedestrian-level sensor network. In addition, classification metrics are calculated to quantify the ability of the model to predict the UTCI heat stress classes as a function of the

surrounding areas by increasing the radii of considered data around the measurement station (Table B1). True Skill Score (TSS), Probability of Detection (POD), and False Alarm Rate (FAR) are used as evaluation metrics. The TSS is defined as follows:

$$\mathrm{TSS} = \frac{a}{\mathrm{a}+\mathrm{c}} - \frac{\mathrm{b}}{b+d} \tag{3}$$

with true positives (a), false positives (b), false negatives (c), and true negatives (d). TSS closer to +1 indicates more accurate prediction, TSS closer to 0 indicates less accurate prediction. The definitions of POD and FAR can be found in Appendix B.

2.5.2. *Significance test*

To distinguish whether the heat stress hours of the three RCP scenarios differ significantly from the historical ERA5-Land data, a significance test is applied. As the heat stress hours data do not follow a normal distribution, the nonparametric paired Wilcoxon signed rank test is used (Hastie et al., 2009). This test is applied in two ways: (1) to test the overall significance between ERA5-Land and the different RCP scenarios and (2) to test the significance of each hexagon (defined by a particular land cover fraction combination) shown in Fig. 4. For (1), the 5.0 km × 2.5 km prediction areas are compared in their entirety and the five different climate models are pooled into one dataset. As the test is paired, each 1 m × 1 m ERA5-Land grid cell is compared with its corresponding grid cell in the RCP data. The significance level of the paired Wilcoxon signed rank test is 0.05 (p-value). In (2), the 100 m × 100 m grid cells are identified for each hexagon from Fig. 4. Each 100 m × 100 m still has a 1 m resolution and for each 100 m × 100 m grid cell the significance is tested individually. However, as each hexagon of Fig. 4 can be assigned up to multiple different 100 m × 100 m grid cells, the p-value must be adjusted to account for the multiple comparison problem (type I error). This is done by dividing the p-value by the number of 100 m × 100 m grid cells per hexagon (Bonferroni correction): For example, if a hexagon is assigned to 10 different 100 m × 100 m grid cells, the p-value is 0.05 / 10 = 0.005. Figure 4b and d show how many of the corresponding grid cells are

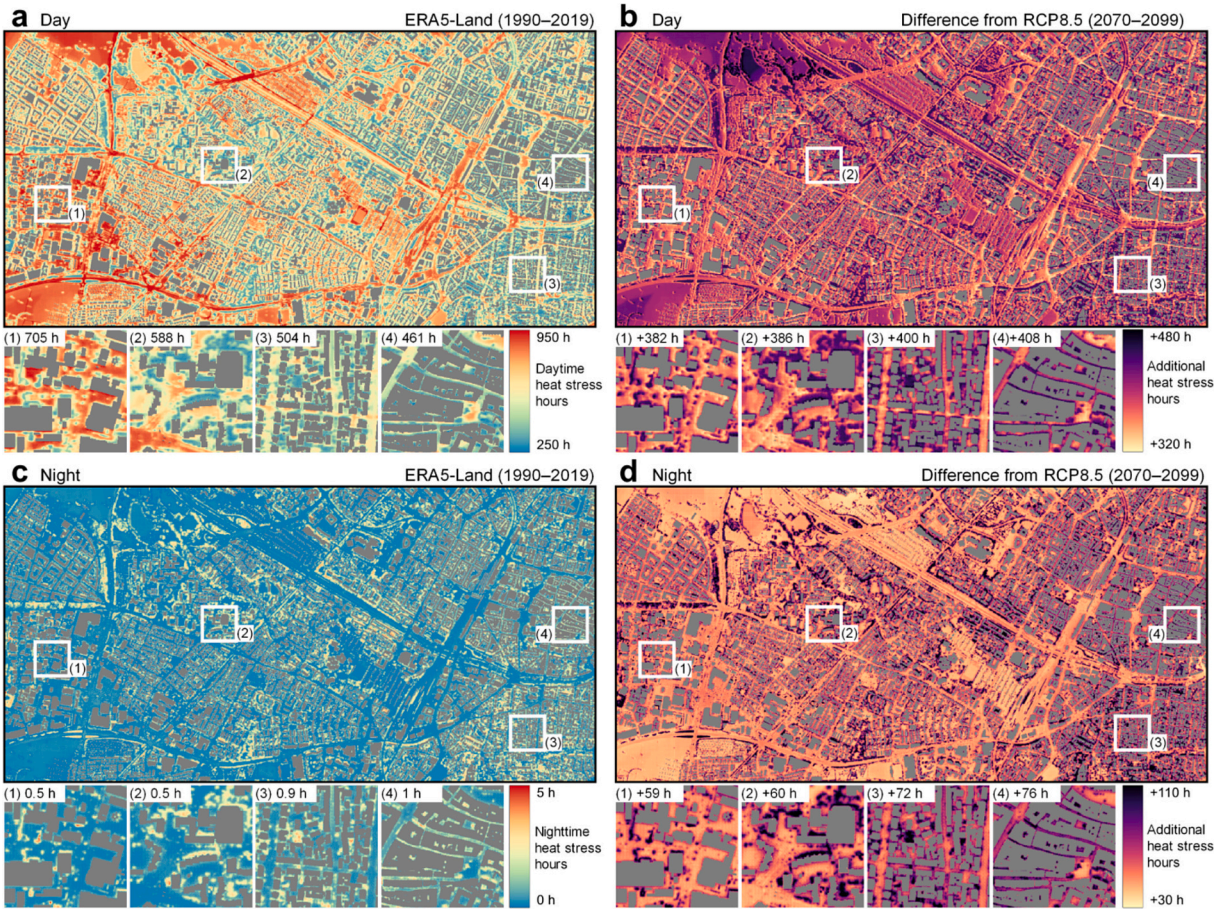

Fig. 3. Mean heat stress hours (UTCI ≥ 26 °C) per year with 1 m resolution for an area of 5.0 km × 2.5 km in Freiburg, Germany. Heat stress hours at pedestrian level modelled by UHTC-NN for the historical period are shown in **a** for daytime and in **c** for nighttime. The additional heat stress hours of the RCP8.5 scenario ensemble downscaling are shown in **b** and **d**. The small panels (1)–(4) represent different neighborhoods with (1) an industrial area (LCZ 8), (2) an open arrangement of mid-rise to large buildings (LCZ 5), (3) an open low-rise residential area (LCZ 6), and (4) a dense arrangement of mid-rise to large buildings (LCZ 2). Building footprints are excluded from calculations and shown in grey.

significant for the RCP8.5 scenario (< 90 %, 90 %–95 %, ≥ 95 %).

3. Results

3.1. Validation of the UHTC-NN

The UHTC-NN is validated in two steps. First, the HTC-NN and UHTC-NN are compared with data from the urban sensor network. Although the HTC-NN has already undergone extensive point validation using data from the urban sensor network (Briegel et al., 2024), the predictions of the HTC-NN and the UHTC-NN are compared with the sensor network data to ensure that the predictions of both models are reasonable and that the UHTC-NN is accurate against not only its parent HTC-NN model, but also against measurements. The respective MAEs of the HTC-NN and UHTC-NN are 1.85 K and 1.83 K, and the respective RMSE are 2.46 K and 2.45 K. The MAE of the UHTC-NN ranges from 1.40 K to 2.72 K across the different sensor stations, and from 1.11 K to 4.01 K across the different test days. These results agree with the findings of Briegel et al. (2024) and demonstrate that the UHTC-NN has a similar ability to predict UTCI as the HTC-NN. TSS analysis of heat stress classes shows that smaller radii result in higher TSS for heat stress in general

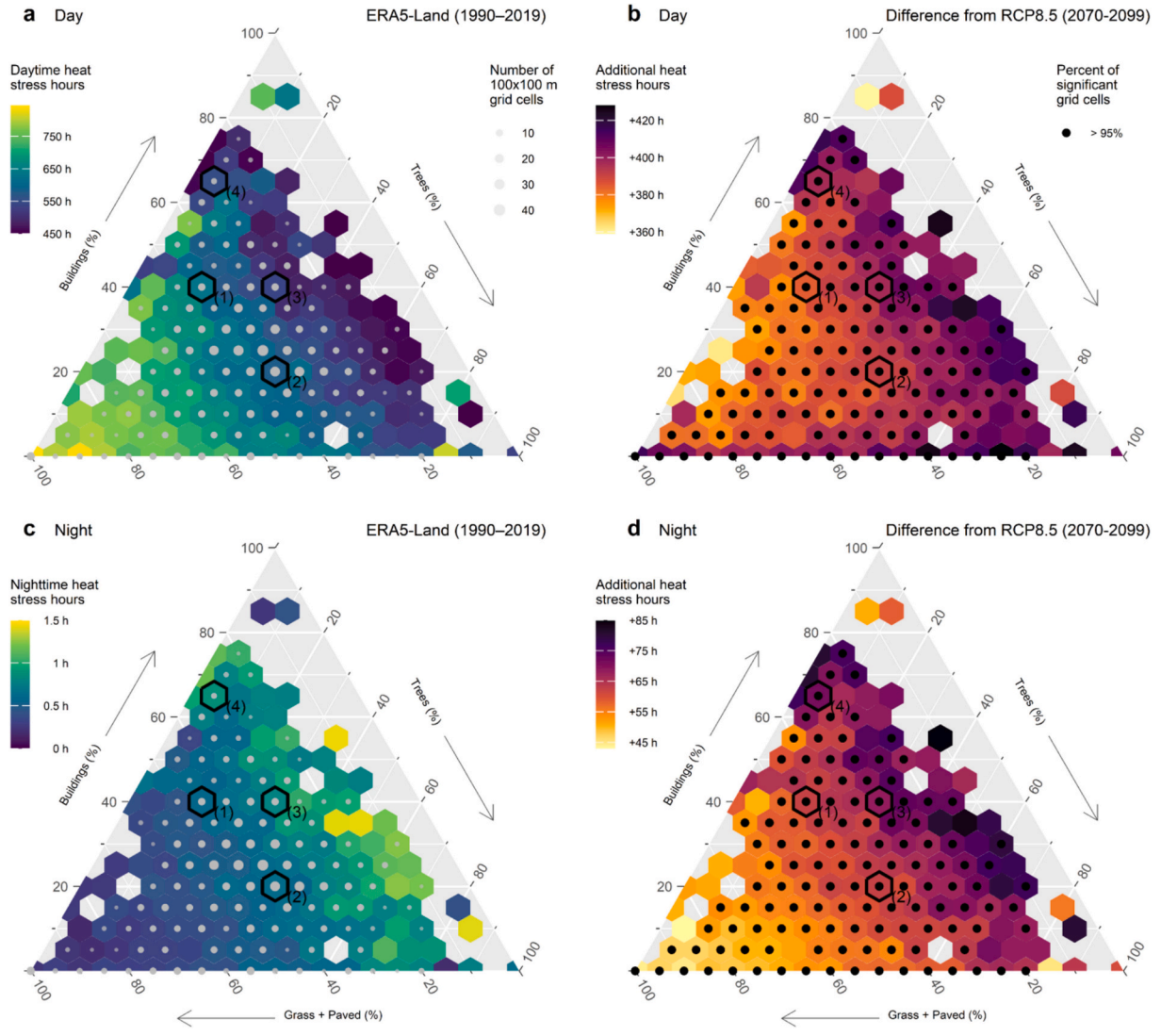

Fig. 4. Average heat stress hours per year (UTCI ≥ 26 °C) and 100 m × 100 m grid cell as function of land cover class fractions depicted in a ternary plot. Each hexagon represents a certain land cover fraction combination and shows the average heat stress hours of all grid cells sharing this land cover fraction combination (bin size is 5 %). The grey dots show the number of grid cells for each hexagon. The black dots show the percentage of significantly different 100 m × 100 m cells in each hexagon (see Methods section). The upper panels (**a** and **b**) show the average heat stress hours for daytime and the lower panels (**c** and **d**) for nighttime. The historical reference period is shown in **a** and **c**, while **b** and **d** show the additional heat stress hours of the RCP8.5 scenario ensemble. The black framed hexagons (1)–(4) correspond to the sub-panels from Fig. 3.

and for strong heat stress (see Table B1). TSS for heat stress in general is 0.78 and TSS for strong heat stress is 0.71 at the radius of 1 m, whereas at a radius of 100 m, TSS is 0.72 for heat stress in general and 0.50 for strong heat stress. TSS for moderate heat stress is quite similar for different radii, ranging from 0.51 for the 1 m radius to 0.54 for the 100 m radius.

In the second validation step, the UHTC-NN and the HTC-NN predictions are compared on an area basis. The overall MAE of all 15 test areas and 30 test days is 0.42 K, while the RMSE is 0.57 K. Figure B1 shows box plots of the RMSE by meteorological season (a), averaged daily cycles by season (b), box plots by test area (c) and by test day (d). There is slight variation in model accuracy between seasons, with an RMSE of around 0.5 K. Errors are lower at night than during the day, and vary more between test days than between test areas. In summer, the highest errors occur in the morning and evening. In spring and autumn, the highest errors occur before and after noon, whereas in winter, there is no clear trend. On average, the UHTC-NN has higher errors during the day than at night.

3.2. Historical heat stress conditions in urban environments

Example heat stress maps for a 5.0 km × 2.5 km area are shown in Fig. 3. The maps show the average hours per year and pixel (m^2) exceeding a UTCI value of 26 °C at pedestrian level (1.3 m a.g.l.), which represents the threshold for heat stress (Błażejczyk et al., 2013), and are hereafter referred to as heat stress hours. Average heat stress hours are differentiated by day (Figs. 3a, b) and night (Figs. 3c, d), and by historical reference period (1990–2019 – Figs. 3a, c) and projected average increase of the downscaled RCP8.5 scenario ensemble (2070–2099 – Figs. 3b, d). Figure 3a illustrates substantial differences and high spatial variability in daytime heat stress hours at the neighborhood and microscale across the city, with values ranging from approximately 250 h to 950 h at a spatial resolution of 1 m. At night, heat stress hours are almost non-existent in the historical period (Fig. 3c), with up to 5 h in selected locations.

Sub-panels (1)–(4) of Fig. 3a-d show map tiles of four neighborhoods with different local climate zones (LCZ) (Stewart and Oke, 2012). Sub-panel (1) represents an industrial area with large buildings, paved surfaces and few trees (LCZ 8), while sub-panels (2) and (3) are residential areas with mature tree stocks (LCZ 5 and 6, respectively), and (4) is the historic city center of Freiburg with a dense mix of mid-rise buildings and low tree coverage. These sub-panels are added to illustrate contrasting neighborhoods within the same city.

The different spatial pattern of daytime and nighttime heat stress hours at the neighborhood scale (sub-plots shown in Fig. 3) can be assessed more systematically in the context of land cover fractions (Fig. 4). For Fig. 4, a 100 m × 100 m grid is superimposed on the heat stress hours maps and heat stress hours are averaged within each grid cell. In addition, land cover fractions (buildings, paved surfaces, grass surfaces, tree canopy coverage) are calculated for each grid cell. Each hexagon represents a particular combination of land cover fractions and shows the average heat stress hours of all grid cells sharing that land cover fraction combination. During the day, a higher proportion of buildings/trees leads to less heat stress hours, while a higher proportion of paved/grass explains more heat stress hours (Fig. 4a). At night, however, the pattern is reversed, with more heat stress hours in neighborhoods with higher building/tree fractions (Fig. 4c). Figure 5 shows hours of heat stress differentiated by UTCI heat stress class: moderate (26 °C ≤ UTCI < 32 °C), strong (32 °C ≤ UTCI < 38 °C), and very strong (UTCI ≥ 38 °C), similar to Fig. 4. The spatial patterns of the heat stress hours across the different stress classes are almost identical in the reference period, with more hours occurring open areas with higher proportion of grass/paved surfaces. However, there is a shift towards an increase in hours as the proportion of building increases from moderate to very strong heat stress.

3.3. Future heat stress conditions change under climate change

By the end of the 21st century, heat stress hours are projected to increase by an average of up to 480 h during the day and up to 110 h at night (Figs. 3b, d). According to the RCP8.5 scenario, nocturnal heat stress will become a common stress factor in the future. Although the average relative increase in daytime heat stress hours is smaller than at night (+63 % vs. +600 %), the average absolute increase is greater during the day (+393 h vs. +61 h). Daytime heat stress for strong and very strong heat stress increases by +172 h (reference: 135 h) and +64 h (reference 7 h), respectively. This equates to percentage increases of 128 % and 914 %, respectively. The increase in heat stress hours varies substantially between neighborhoods for both day and night, with some areas experiencing smaller or larger changes. The increase pattern differs between day and night, with greater variability observed during the day. In the reference period, daytime heat stress hours decrease from sub-panels (1) to (4) in Fig. 3a, but heat stress hours increase from (1) to (4) under the RCP8.5 scenario (Fig. 3b). Conversely, current nighttime heat stress hours increase from (1) to (4), with the city center experiencing the highest number of heat stress hours. Under the RCP8.5 scenario, the increase in nighttime heat stress hours mirrors the daytime trend, increasing from (1) to (4).

Figure 4b and d show that the patterns of additional heat stress hours as a function of land cover class fractions under the RCP8.5 scenario are nearly identical for both day and night. Results for RCP2.5 and RCP4.5 are shown in Appendix C (Figs. C1, C2). The increase in additional heat stress hours is higher in areas with more buildings/trees and lower in open areas with fewer buildings/trees. However, in areas with sparse building density, the increase in additional heat stress hours is more pronounced at night compared to daytime. When distinguishing between the different heat stress classes (Fig. 5), the increase patterns are almost opposite for moderate and very strong heat stress (Figs. 5b, f). While hours with moderate heat stress increase most in areas with a higher proportion of buildings or trees, hours with very strong heat stress increase particularly in open areas with a high proportion of grass and paved surfaces (Fig. C3). The pattern of increases for strong heat stress is intermediate, with the highest increases occurring in areas with a low proportion of buildings (Fig. 5d).

Figure 6 illustrates the same relationship as Fig. 4, but in a two-dimensional form that allows to distinguish between grass and

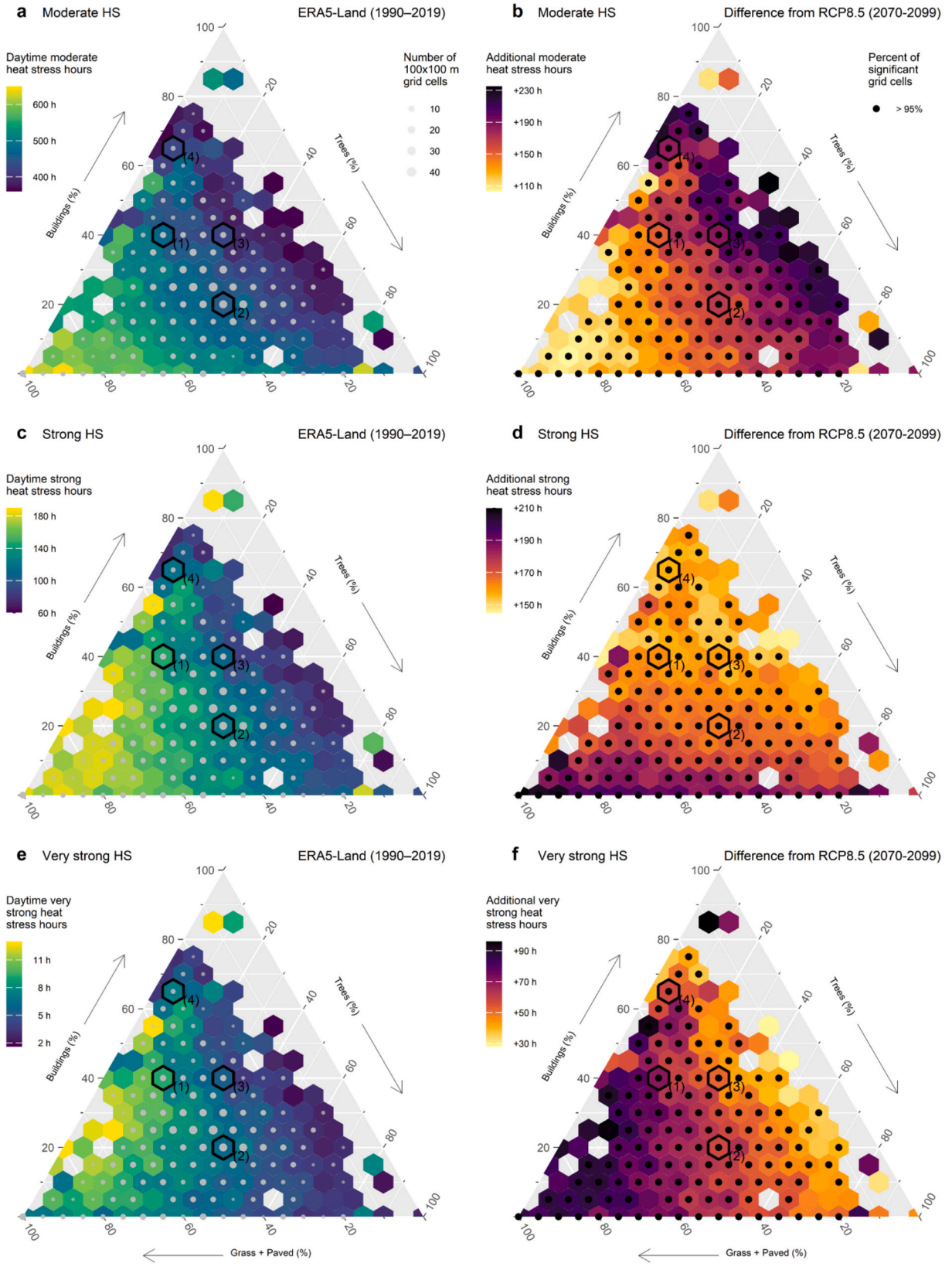

(caption on next page)

Fig. 5. Average heat stress hours distinguished by UTCI stress classes per year and 100 m × 100 m grid cell as function of land cover class fractions depicted in a ternary plot similar to Fig. 4. The panels **a** and **b** show the average 'moderate heat stress' (Moderate HS) hours, **c** and **d** the average 'strong heat stress' (Strong HS) hours, and **e** and **f** the average 'very strong heat stress' (Very strong HS) hours. All panels show the daytime situation. The historical reference period is shown in **a**, **c**, and **e**, while **b**, **d**, and **f** show the additional heat stress hours of the RCP8.5 scenario ensemble. The black framed hexagons (1)–(4) correspond to the sub-panels from Fig. 3.

paved fractions. Figure 6b and d show that the proportion of grass has an inverse effect on the additional heat stress hours between day and night: during the day, the additional heat stress hours increase as the proportion of grass increases, whereas at night the additional heat stress hours decrease as the proportion of grass increases. In addition, Figs. 6c and d demonstrate that the relationships between land cover fractions and (additional) nighttime heat stress hours follows the same pattern for both the reference period and the projected increase under RCP8.5. However, the relationships between (additional) daytime heat stress hours and the building, tree, and paved fractions differ between the reference period and the projected increase under RCP8.5 (Figs. 6a, b). The spatial patterns in Fig. 5b, d, which show fewer hours for low proportions of buildings and trees, are reflected in the initial minimum of additional heat

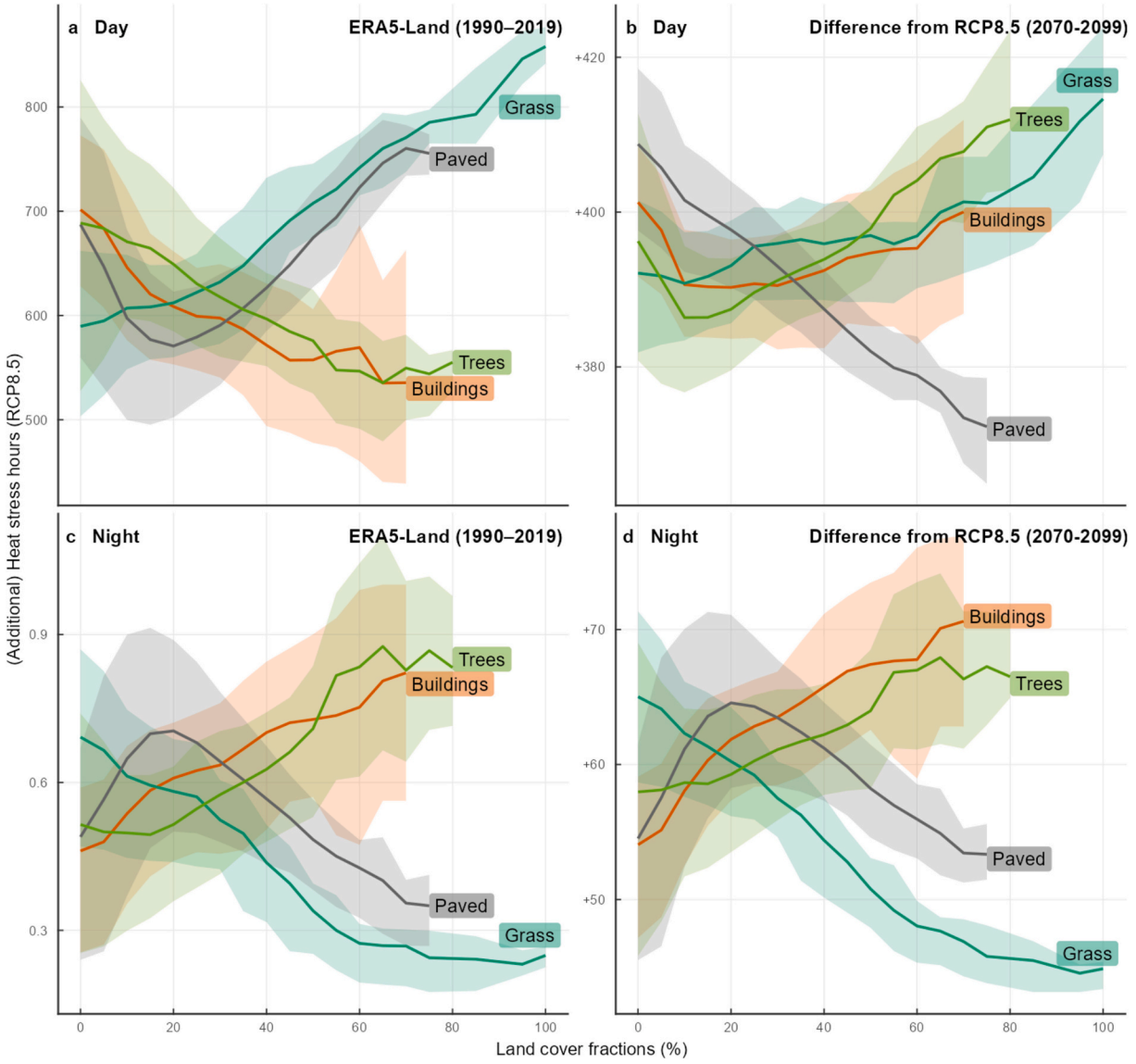

Fig. 6. Average heat stress hours (UTCI ≥ 26 °C) per year and 100 m × 100 m grid cell as function of land cover class fractions (bin size is 5 %). The upper panels (**a** and **b**) show the average heat stress hours for daytime and the lower panels (**c** and **d**) for nighttime. The historical reference period is shown in **a** and **c**, while **b** and **d** show the additional heat stress hours of the RCP8.5 scenario ensemble. Note that a minimum of three areas per bin are used as thresholds and that the scales of the y-axes differ between the subplots. Shaded areas are the 95 % confidence intervals of the spatial variability.

stress hours for building and tree proportions in Fig. 6b.

Figure 7 shows the additional heat stress hours under RCP8.5 as a function of the reference period heat stress hours differentiated by UTCI stress classes. For moderate heat stress during the day, areas with more heat stress hours under the current climatic conditions experience a smaller increase of additional heat stress hours, while areas with fewer hours experience a larger increase (Fig. 7a). For strong heat stress there is no clear trend. However, for very strong heat stress, a clear trend emerges: areas with more hours of very strong heat stress during the reference period experience a greater increase in additional very strong heat stress hours than areas with fewer hours (Fig. 7b). The same pattern is observed at night: areas with more hours of heat stress experience a greater increase in additional heat stress hours (Fig. 7c).

4. Discussion

Validation of UHTC-NN shows a comparable accuracy to other thermal comfort models (Krayenhoff et al., 2021; Meili et al., 2021; Nice et al., 2022; Briegel et al., 2024). Its high accuracy and rapid computation allow efficient downscaling of multi-decadal reanalysis data or climate ensembles on a 3-hourly resolution. This enables robust assessment of the spatial heterogeneity of projected climate change signals for entire cities.

4.1. Historical heat stress

The downscaling of the ERA5-Land-reanalysis data reveals significant intra-urban variability in heat stress (Fig. 3), highlighting the need to distinguish between daytime and nighttime heat hotspots (Wang et al., 2021). The microscale patterns of heat stress hours are strongly influenced by urban morphology (Fig. 3). At a coarser level of aggregation (100 m), average heat stress hours are closely

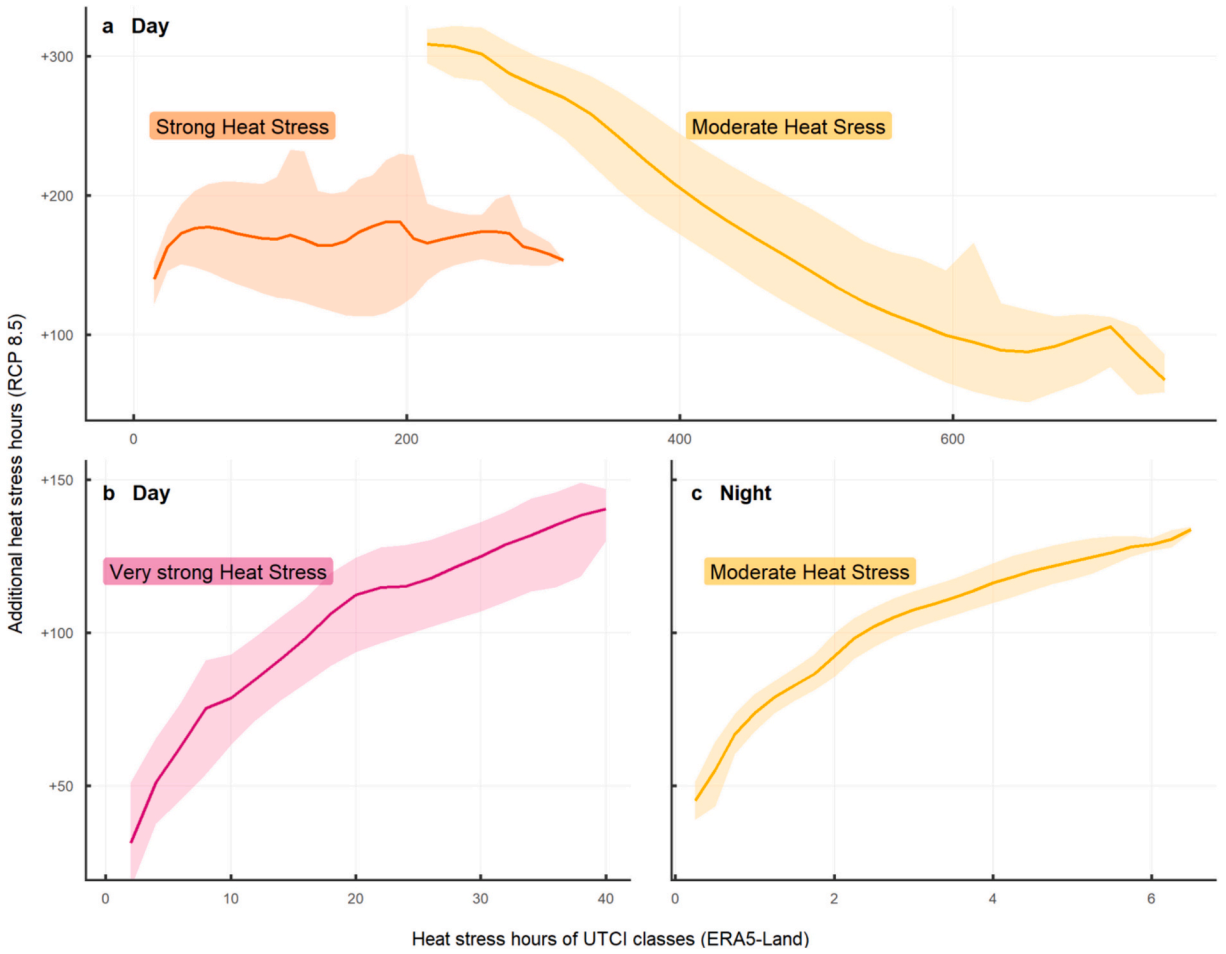

Fig. 7. Additional heat stress hours of the RCP8.5 scenario ensemble downscaling as a function of heat stress hours in the historical reference period. Panel **a** show the daytime conditions for moderate and strong heat stress, while panel **b** shows very strong heat stress. Panel **c** shows moderate heat stress at night. The colors represent UTCI heat stress classes: moderate heat stress (26 °C ≤ UTCI < 32 °C), strong heat stress (32 °C ≤ UTCI < 38 °C), and very strong heat stress (UTCI ≥ 38 °C). Shaded areas are the 95 % confidence intervals of the spatial variability.

correlated with land cover fractions (Figs. 4, 6). Different types of land cover lead to a day-night contrast of heat stress hours, mainly due to shading, radiation reflection/emission, and ventilation effects. In particular, daytime heat stress is significantly reduced by shading, and areas with a higher proportion of trees or buildings experience fewer heat stress hours than open areas (Middel et al., 2016). On hot, solar radiation-intensive days, heat stress is primarily driven by solar radiation, with shading reducing T_{mrt} and hence UTCI. In contrast, the number of heat stress hours at night is higher in areas with more trees or buildings compared to open areas as long-wave radiation trapping becomes the dominant process: the three-dimensional nature of cities (buildings and trees) increases the surface area, leading to higher longwave radiation emissions towards the pedestrian level and thus to higher T_{mrt} (Allegrini et al., 2012). The combination of radiation trapping and reduced ventilation increases nighttime heat stress in street canyons with large tree canopies. This day-night variation highlights the challenge of balancing daytime shading with nighttime radiation trapping and ventilation in climate-sensitive design.

The results of this study align with those of comparable studies that have investigated pedestrian-level thermal comfort at a building-resolved scale. During the daytime, shading is the main factor in describing small-scale variability (Crank et al., 2020; Middel et al., 2021), whereas at night, radiation trapping and reduced near-surface T_a cooling are important factors (Masson et al., 2020; Weeding et al., 2024).

4.2. Future heat stress

The future increase in heat stress hours, similar to the current spatial variability, is unevenly distributed across the city, with distinct spatial patterns at the neighborhood scale and at the microscale for both day and night and across different heat stress classes (Fig. 3). The average absolute increase in general heat stress hours during the day (+393 h) is significantly higher than at night (+61 h) for RCP8.5. Both RCP8.5 and RCP4.5 show a significant increase over the entire area. However, the RCP2.6 scenario illustrates the need for a combined analysis incorporating climate, spatial heterogeneity, and day/night comparisons (cf. Figs. C1 and C2), where both increases and decreases in heat stress hours occur as a function of land cover fractions. The differences in additional daytime heat stress hours between areas with more buildings or trees and open areas are mainly due to shading. While T_a will increase with projected climate change, solar radiation is expected to remain constant (Table A1). Consequently, the increase in T_a will raise the UTCI baseline in both shaded and sunlit areas. As open areas already experience more heat stress hours, there is less capacity for further increases (Figs. 4a, 5a). However, this does not imply that open areas will experience less heat stress than shaded areas in future. The spatial pattern of heat stress from the reference period will persist, and there will be a shift towards more extreme heat stress classes. The overall distribution of general heat stress hours will become narrower. When differentiating between heat stress classes, the difference in increase between the UTCI classes can be explained in a similar way. Areas that are already frequently exposed to very strong heat stress during the reference period are also much more often exposed to moderate heat stress (Figs. 5a,c,e). This means that these hotspot areas experience a shift between the UTCI stress classes, with a smaller increase in moderate heat stress but a larger increase in very strong heat stress (Figs. 5b,d,f, and 7). Most of the shaded areas will only experience a substantial increase in the moderate and strong heat stress class. At night, areas currently experiencing higher levels of heat stress (more buildings/trees) will face even larger increases in additional heat stress hours compared to areas with lower current levels of heat stress (more grass/paved) due to increased nighttime T_a, and thus increased T_{mrt} by radiation trapping (Figs. 3, 4). In open areas the increase in UTCI is mainly due to higher T_a. As a result, the distribution of heat stress hours at night becomes wider, in contrast to the narrower distribution observed during the day. In conclusion, during the day, ‘cooler’ areas experience a larger absolute and relative increase in heat stress hours, while ‘hotter’ areas show a smaller increase, but with a higher proportion of (very) strong heat stress. At night, the trend is reversed, with ‘hotter’ areas experiencing larger increases and ‘cooler’ areas showing smaller increases. Unprecedented extreme daytime heat stress will show increased heterogeneity, analogous to nighttime heat stress.

There are not many studies that have conducted comprehensive spatial downscaling of climate ensembles to a building-resolved scale. Weeding et al. (2024) used SOLWEIG to downscale an RCP8.5 climate ensemble to a 1 m resolution for a 150 m × 150 m domain in Tasmania. They found a median increase in hours of strong and very strong heat stress of 74 % and 125 %, respectively, from the 1990–2005 period to the 2040–2059 period. While the two study areas cannot be compared directly and our study uses the period 2070–2099 as the future scenario (+128 % and +914 % for strong and very strong heat stress respectively), the observed trends in both studies suggest a significant rise in heat stress, particularly towards the end of the century.

4.3. Potential limitations

Downscaling climate ensembles to a building resolved scale holds several potential sources of uncertainty such as accuracy of the chosen modelling/downscaling approach, quality of meteorological and spatial data, and assumption made to represent future urban structures.

Although we demonstrated that the proposed models are as accurate as comparable urban climate models, their accuracy is still limited by the data on which they are trained. As statistical models, incorporating machine- and deep learning models, are capable of interpolation, extrapolation must be approached with caution. For this reason, this research focuses on general heat stress hours rather than extreme values, as only a few hours with these extremes occurred during the training period. The same is true of spatial urban morphometric data. As we trained and evaluated the model in Freiburg, Germany, the findings are specific to Freiburg and may differ for cities in other climate zones and with different urban structures. However, as other studies have found similar effects of urban morphology on heat stress (Weeding et al., 2024), the conclusion drawn should be valid in principle.

In this modelling approach, the current urban morphology and vegetation are ‘frozen’, and no assumptions are made about future

changes in land use or ecosystem functions. While this approach leaves potential adaptation actions unconsidered, it preserves the current tree canopy and vegetation structure and thus the ecosystem functions, which will most likely differ by the end of the 21st century (e.g., tree mortality has already increased in Germany in recent years due to droughts and extreme temperatures - Haberstroh et al., 2022; Schiefer et al., 2024). In addition, not every pixel may be correctly classified in the context of land cover. However, we think this should not influence the general trend when we compare current to future stress. These and other caveats should be addressed in future studies.

5. Conclusion

Our study presents a novel deep learning model UHTC-NN, designed to model human thermal comfort (UTCI) in complex urban environments. This model provides rapid, high-resolution predictions of two-dimensional UTCI fields at pedestrian-level, enabling systematic and quantitative analysis of heat stress in urban environments. By downscaling extensive meteorological datasets, including reanalysis and climate projections, to a building-resolved scale, UHTC-NN provides detailed insights into the spatial patterns of urban heat stress. We demonstrate the model's capabilities by applying it to downscale a CMIP5 climate model ensemble to 1 m resolution for a 5.0 km $\times$ 2.5 km area in Freiburg, Germany.

Our findings reveal significant increases in heat stress hours under the RCP4.5 and RCP8.5 scenarios, with the climate signal as the dominant effect, while under the RCP2.6 scenario increases and some decreases in heat stress hours occur, with urban land cover as the dominant effect. Nevertheless, large intra-urban variability in heat stress hours is found for both the reference period (1990–2019) and the projected future changes (2070–2099), which underlines the need of high-resolution prediction models like UHTC-NN for mapping heat exposure in urban environments. This spatial variability is closely related to land cover fractions and shows inverse day/night spatial patterns. Future daytime general heat stress will exhibit reduced spatial heterogeneity, while nighttime heat stress and daytime extremes will show increased spatial heterogeneity. The high-resolution UTCI predictions generated by UHTC-NN mark a significant advance in data-driven heat stress modelling for complex urban environments.

A combined analysis of climate change impacts, complex urban structures, and diurnal (day/night) patterns, which can be examined simultaneously by this approach, is required for a holistic understanding of these processes. Once validated and adapted for use in other cities, UHTC-NN has the potential for global applications, significantly improving our ability to address and mitigate urban heat hotspots in the face of climate change. Such comprehensive insights open a wide range of possibilities for urban planning, from the evaluation of adaptation measures and design alternatives, to the assessment of critical infrastructure, and the advancement of research on urban-environment-heat interactions - all while consistently taking into account the effects of climate change.

Code availability

Code of the UHCT-NN can be found here: https://github.com/SimonSchrodi/UTCI.

CRediT authorship contribution statement

Ferdinand Briegel: Validation, Data curation, Visualization, Software, Writing – original draft, Methodology, Conceptualization. **Simon Schrodi:** Software, Methodology, Writing – review & editing. **Markus Sulzer:** Data curation, Writing – review & editing. **Thomas Brox:** Conceptualization, Funding acquisition, Supervision, Writing – review & editing. **Joaquim G. Pinto:** Funding acquisition, Writing – review & editing, Supervision. **Andreas Christen:** Funding acquisition, Writing – review & editing, Supervision, Conceptualization, Project administration.

Declaration of competing interest

The authors declare that they have no conflict of interest.

Data availability

Data will be made available on request.

Acknowledgements

The model development and evaluation were funded by the German Federal Ministry for the Environment, Nature Conservation and Nuclear Safety (BMU) on the basis of a resolution of the German Bundestag as part of the 'KI-Leuchtturm' project 'Intelligence for Cities' (I4C). Validation data (sensor network) used in this research were collected as part of the ERC Synergy Grant 'urbisphere' project, funded by the European Research Council (ERC-SyG) within the European Union's Horizon 2020 research and innovation program under grant agreement no. 855005. Spatial data (DEM / DSM) was provided by the administration of the city of Freiburg. We gratefully acknowledge Matthias Zeeman, Marvin Plein, Gregor Feigel, Andreas Matzarakis, Felix Baab, and Dirk Redepenning from the University of Freiburg for the design, installation and operation of the sensor network, the data management, and for providing the data. We would also like to thank Christiane Felder for the management of the I4C project. F.B. is partially funded by the Helmholtz program "Changing Earth" at KIT. J.G.P. thanks the AXA Research Fund for support.

Appendix A. Data and methods

Table A1
Metrics of different meteorological input variables for the reference period from 1990 to 2019 (ERA5-Land) and the climate projections from 2070 to 2099 distinguished by RCPs.

Scenario	T_a		Kdown		Ldown		RH	U
	mean	mean of daily maximum	mean	mean of daily maximum	mean	mean of daily maximum	mean	mean
	(°C)	(°C)	(W m^{-2})	(W m^{-2})	(W m^{-2})	(W m^{-2})	(%)	(m s^{-1})
ERA5-Land	9.5	13.5	140	476	309	337	78.7	2.0
RCP2.6	10.2	14.4	137	440	315	340	79.5	2.5
RCP4.5	11.3	15.4	135	434	322	347	79.4	2.6
RCP8.5	13.2	17.3	135	434	334	359	78.1	2.6

Table A2
Hyper-parameter of the U-Net model.

Hyper-parameter	Value
Loss function	L1
Optimizer	AdamW
Learning rate	0.001
Weight decay	1e-3
Learning rate scheduler	cosine annealing

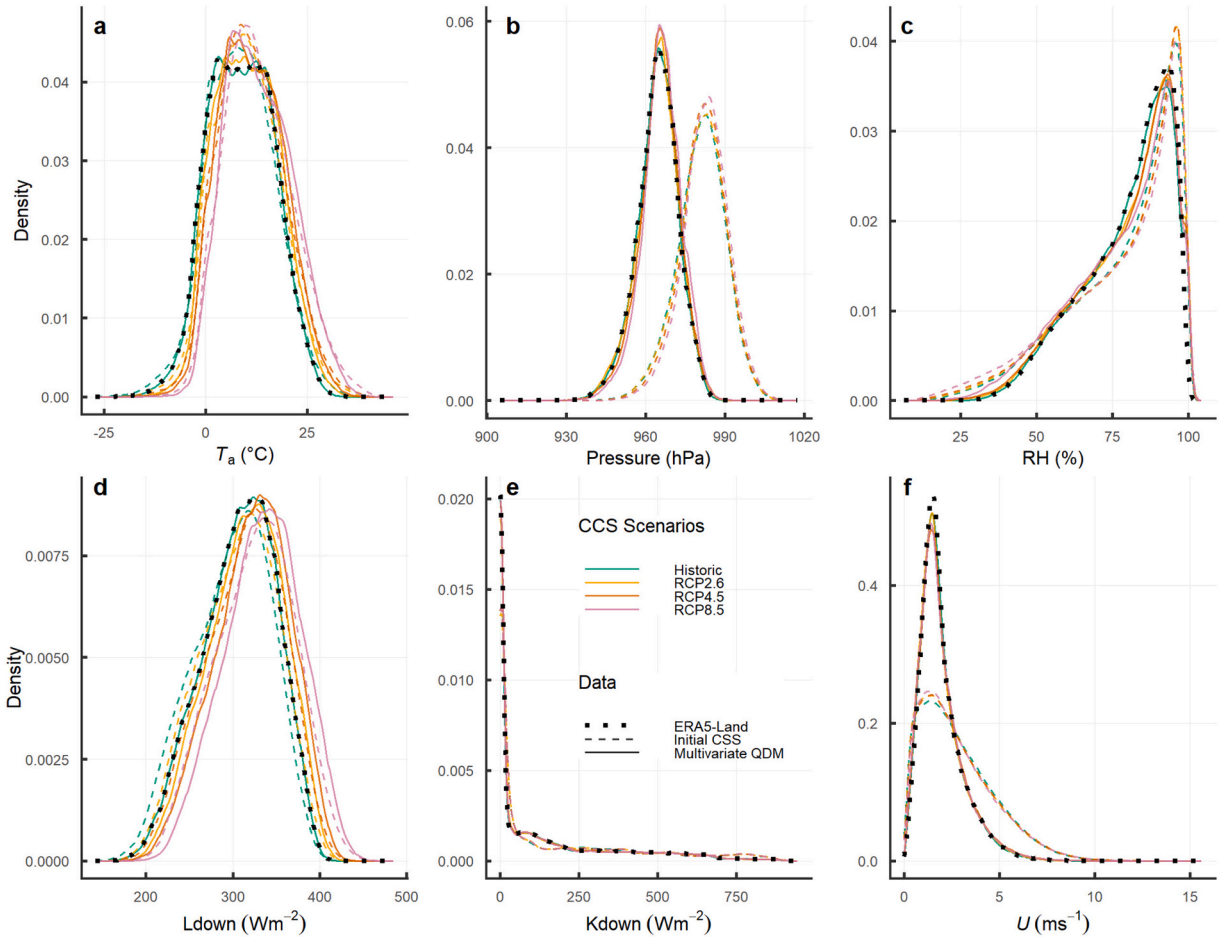

Fig. A1. Density plots of the initial CCS scenario data (2070–2099), the multivariate bias corrected data (2070–2099), and the ERA5-Land data (1990–2019). Panel **a** shows the results for T_a, **b** for Pressure, **c** for RH, **d** for Ldown, **e** for Kdown, and **f** for U.

Appendix B. Evaluation of the UHTC-NN

Impact of spatial data inaccuracy and spatial correlation

In addition to evaluating the UHTC-NN on measurement data, this section shows and discusses the effect of the accuracy of the spatial data, edge effects of the model predictions, and how RMSE is influenced by increasing distance to the measurement stations of the sensor network.

As spatial data such as building and vegetation DSMs are subject to uncertainty, we evaluated the impact of these inaccuracies. According to the data provider, the City of Freiburg and the State of Baden-Württemberg, the DSM data has an error range of ±0.15 m. We simulated the UTCI for one day with hourly resolution in one of the test areas. We found that the differences ranged from -0.0015 K to 0.0006 K, which is negligible. The edge effects of the model predictions are shown in Fig. B2, with averaged RMSE map across all test areas and days (a) and with RMSE as a function of the distance to the edges. It can be seen that RMSE is slightly increased closer to the edges. Although, this margin is quite small, the predictions are adjusted to account for these effects (see methods section).

Increasing the radius used to capture data for evaluation on the sensor network results in an increasing RMSE trend, from 2.20 °C for a 1 m radius to 2.55 °C for a 100 m radius (5 m radius: 2.22 °C; 10 m radius: 2.28 °C; 50 m radius: 2.44 °C).

Definition of Probability of Detection (POD) and False Alarm Rate (FAR)

True positives (a), false positives (b), false negatives (c), and true negatives (d).

$$\mathrm{POD} = \frac{a}{\mathrm{a} + \mathrm{c}} \tag{4}$$

$$\mathrm{FAR} = \frac{b}{\mathrm{a} + \mathrm{b}} \tag{5}$$

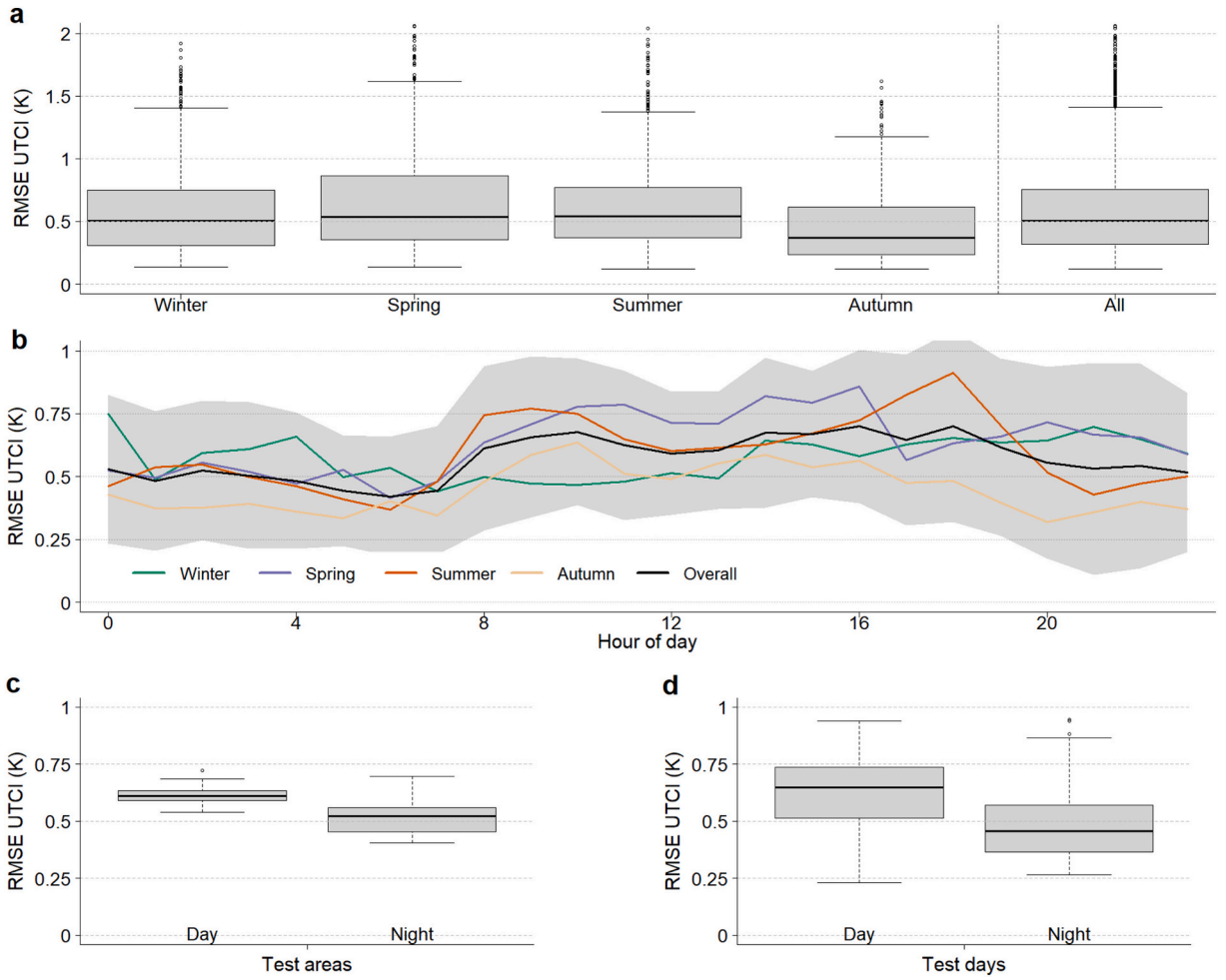

Fig. B1. Evaluation of the UHTC-NN on its parent model proposed by Briegel et al., 2024**.** Boxplots of root mean square error (RMSE) by season are shown in **a**. RMSE as a function of time of day for different seasons is shown in **b**. The differences between day and night are shown in **c** and **d**, while **c** shows the averages by test areas and **d** by test days.

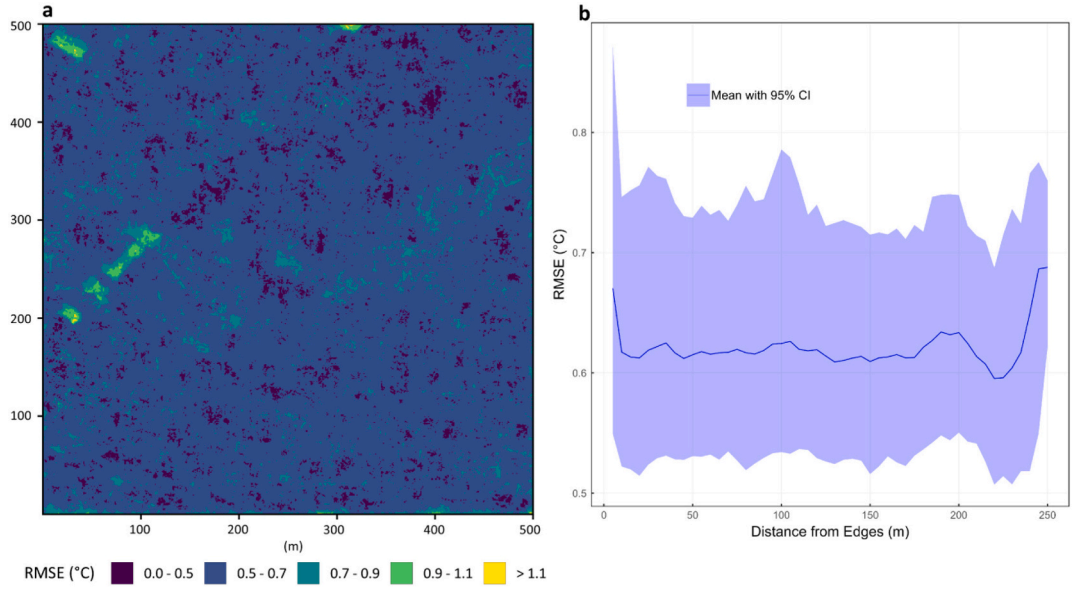

Fig. B2. Spatial mapping of prediction errors. RMSE averaged over all test areas and test days (**a**). RMSE as a function of distance to the edge of the 500 m × 500 m grid (**b**).

Table B1

True Skill Score (TSS), Probability of Detection (POD), and False Alarm Rate (FAR) of the UHTC-NN compared to measured data of the sensor network. Results are differentiated by different radii of considered simulated values of the UHTC-NN for comparison. Heat stress is defined as UTCI ≥26 °C, moderate heat stress as 32 °C > UTCI ≥26 °C, and strong heat stress as UTCI ≥32 °C.

UHTC-NN				
Radius (m)	UTCI stress class	TSS	POD	FAR
1	Heat stress	**0.78**	**0.80**	0.16
	Moderate heat stress	0.51	0.54	0.35
	Strong heat stress	**0.71**	**0.74**	0.43
5	Heat stress	**0.78**	**0.80**	0.16
	Moderate heat stress	0.51	0.55	0.35
	Strong heat stress	0.69	0.71	0.43
10	Heat stress	0.76	0.79	0.15
	Moderate heat stress	0.51	0.55	**0.34**
	Strong heat stress	0.69	0.70	0.40
50	Heat stress	0.72	0.74	0.13
	Moderate heat stress	0.53	0.57	0.35
	Strong heat stress	0.56	0.57	0.30
100	Heat stress	0.72	0.74	**0.11**
	Moderate heat stress	**0.54**	**0.57**	0.35
	Strong heat stress	0.50	0.51	**0.28**

Appendix C. Additional Results

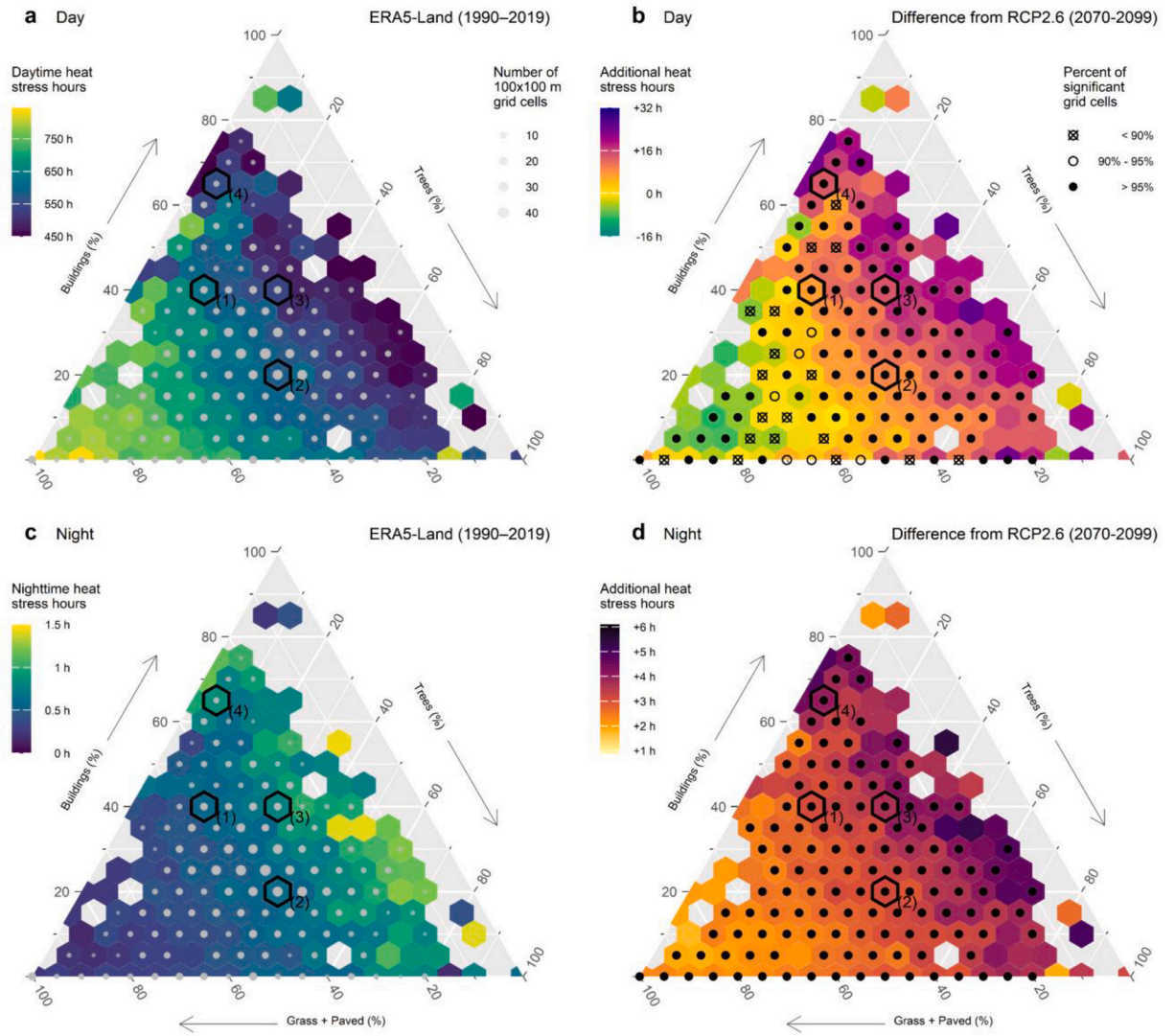

Fig. C1. Average heat stress hours per year (UTCI $\geq$ 26 °C) and 100 m $\times$ 100 m grid cell as function of land cover class fractions depicted in a ternary plot for the RCP2.6 scenario. Each hexagon represents a certain land cover fraction combination and shows the average heat stress hours of all grid cells sharing this land cover fraction combination (bin size is 5 %). The grey dots show the number of grid cells for each hexagon. The black dots show the percentage of significantly different cells in each hexagon (see Methods section). The upper panels (**a** and **b**) show the average heat stress hours for daytime and the lower panels (**c** and **d**) for nighttime. The period 1991–2020 is shown in **a** and **c**, while **b** and **d** show the additional heat stress hours of the RCP2.6 scenario ensemble downscaling (2070–2099). The black framed hexagons (1)–(4) correspond to the sub-panels from Fig. 3.

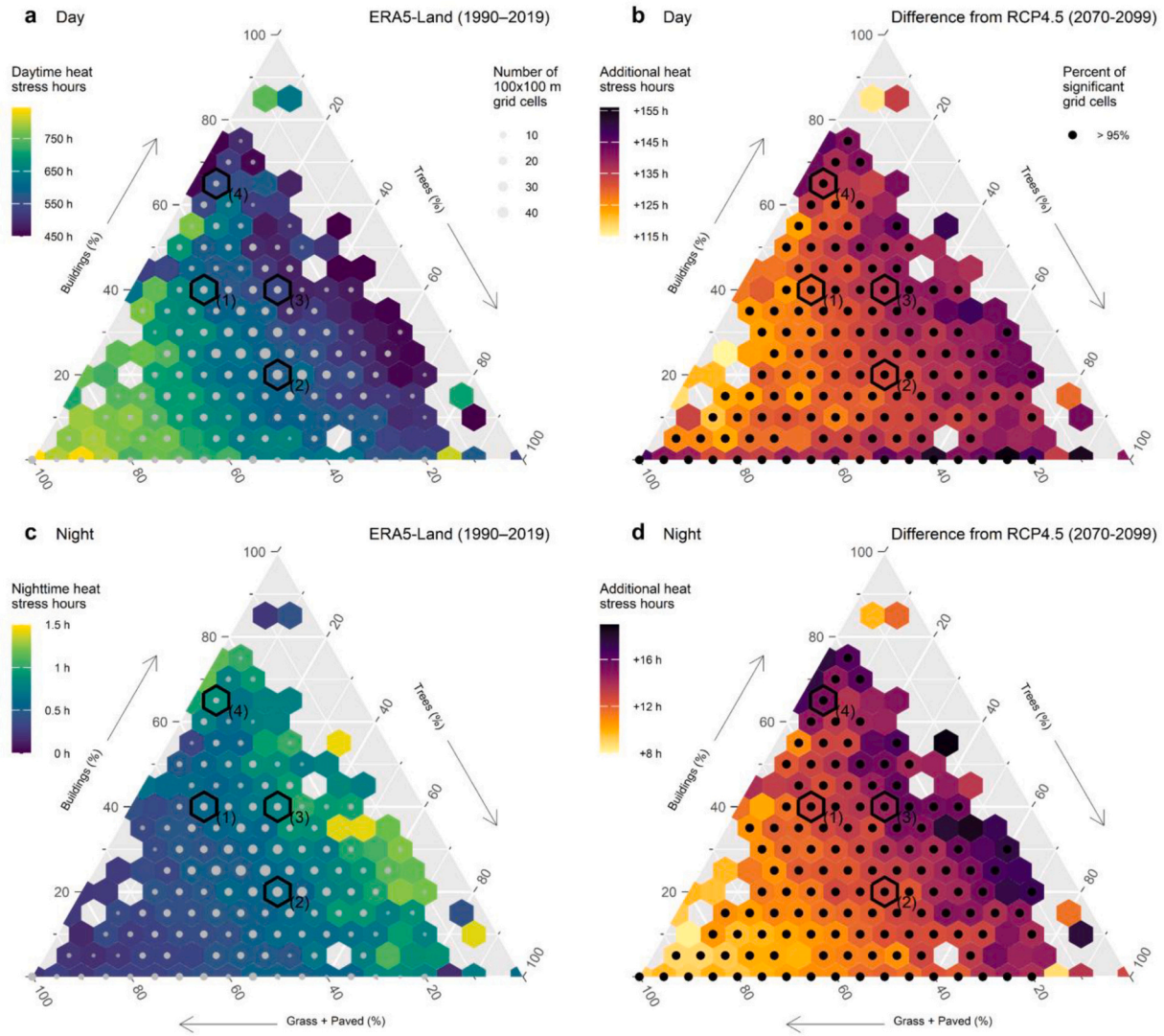

Fig. C2. Average heat stress hours per year (UTCI $\geq$ 26 °C) and 100 m $\times$ 100 m grid cell as function of land cover class fractions depicted in a ternary plot for the RCP4.5 scenario. Each hexagon represents a certain land cover fraction combination and shows the average heat stress hours of all grid cells sharing this land cover fraction combination (bin size is 5 %). The grey dots show the number of grid cells for each hexagon. The black dots show the percentage of significantly different cells in each hexagon (see Methods section). The upper panels (**a** and **b**) show the average heat stress hours for daytime and the lower panels (**c** and **d**) for nighttime. The period 1991–2020 is shown in **a** and **c**, while **b** and **d** show the additional heat stress hours of the RCP4.5 scenario ensemble downscaling (2070–2099). The black framed hexagons (1)–(4) correspond to the sub-panels from Fig. 3.

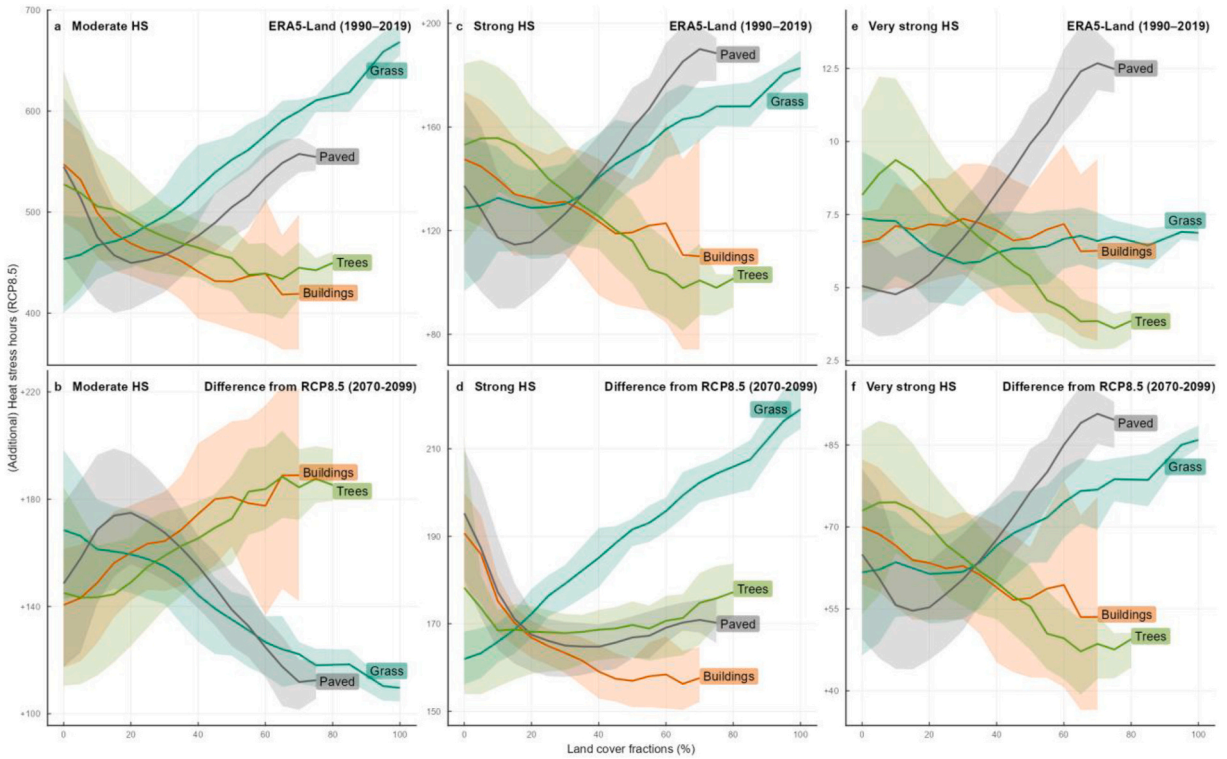

Fig. C3. Average heat stress hours distinguished by UTCI stress classes per year and 100 m × 100 m grid cell as function of land cover class fractions (bin size is 5 %). The upper panels (**a**, **c**, and **e**) show the average heat stress hours for the reference period and the lower panels (**b**, **d**, and **f**) the additional heat stress hours of the RCP8.5 scenario ensemble. Note that a minimum of three areas per bin are used as thresholds and that the scales of the y-axes differ between the subplots. Shaded areas are the 95 % confidence intervals of the spatial variability. All sub-plots only show the daytime situation.

References

Allegrini, J., Dorer, V., Carmeliet, J., 2012. Influence of the urban microclimate in street canyons on the energy demand for space cooling and heating of buildings. Energ. Buildings 55, 823–832. https://doi.org/10.1016/j.enbuild.2012.10.013.

Aminipouri, M., Rayner, D., Lindberg, F., Thorsson, S., Knudby, A.J., Zickfeld, K., Middel, A., Krayenhoff, E.S., 2019. Urban tree planting to maintain outdoor thermal comfort under climate change: the case of Vancouver's local climate zones. Build. Environ. 158, 226–236. https://doi.org/10.1016/j.buildenv.2019.05.022.

Barriopedro, D., Fischer, E.M., Luterbacher, J., Trigo, R.M., García-Herrera, R., 2011. The hot summer of 2010: redrawing the temperature record map of Europe. Science 1979 (332), 220–224. https://doi.org/10.1126/science.1201224.

Barriopedro, D., García-Herrera, R., Ordóñez, C., Miralles, D.G., Salcedo-Sanz, S., 2023. Heat waves: physical understanding and scientific challenges. Rev. Geophys. 61. https://doi.org/10.1029/2022RG000780.

Best, M.J., Grimmond, C.S.B., 2015. Key conclusions of the first international urban land surface model comparison project. Bull. Am. Meteorol. Soc. 96, 805–819. https://doi.org/10.1175/BAMS-D-14-00122.1.

Błażejczyk, K., Jendritzky, G., Bröde, P., Fiala, D., Havenith, G., Epstein, Y., Psikuta, A., Kampmann, B., 2013. An introduction to the universal thermal climate index (UTCI). Geogr. Pol. 86, 5–10. https://doi.org/10.7163/GPol.2013.1.

Briegel, F., Christen, A., 2025. Land cover classes for Freiburg. Germany (Dataset). https://doi.org/10.5281/zenodo.14855706.

Briegel, F., Makansi, O., Brox, T., Matzarakis, A., Christen, A., 2023. Modelling long-term thermal comfort conditions in urban environments using a deep convolutional encoder-decoder as a computational shortcut. Urban Clim. 47, 101359. https://doi.org/10.1016/j.uclim.2022.101359.

Briegel, F., Wehrle, J., Schindler, D., Christen, A., 2024. High-resolution multi-scaling of outdoor human thermal comfort and its intra-urban variability based on machine learning. Geosci. Model Dev. 17, 1667–1688. https://doi.org/10.5194/gmd-17-1667-2024.

Cannon, A.J., 2016. Multivariate Bias correction of climate model output: matching marginal distributions and Intervariable dependence structure. J. Climate 29, 7045–7064. https://doi.org/10.1175/JCLI-D-15-0679.1.

Cannon, A.J., 2018. Multivariate quantile mapping bias correction: an N-dimensional probability density function transform for climate model simulations of multiple variables. Climate Dynam. 20, 31–49.

Cannon Alex, J., 2023. MBC: multivariate Bias correction of climate model outputs - R package version 0.10-6.

Cissé, G., McLeman, R., Adams, H., Aldunce, P., Bowen, K., Campbell-Lendrum, D., Clayton, S., Ebi, K.L., Hess, J., Huang, C., Liu, Q., McGregor, G., Semenza, J., Tirado, M.C., 2022. Health, Wellbeing, and the Changing Structure of Communities. In: Pörtner, H.-O., Roberts, D., Fischlin, A., Howden, M., Méndez, C., Pereira, J.J., Sánchez-Rodríguez, R.A., Semenov, S., Yanda, P., Zatari, T.M. (Eds.), Climate Change 2022: Impacts, Adaptation and Vulnerability. Contribution of Working Group II to the Fifth Assessment Report of the Intergovernmental Panel on Climate Change. Cambridge University Press, Cambridge, UK. In Press.

City of Freiburg im Breisgau, 2021. LIDAR data.

Copernicus Climate Change Service Climate Data Store, 2019. CORDEX regional climate model data on single levels. Copernicus Climate Change Service (C3S) Climate Data Store (CDS) [WWW Document].

Crank, P.J., Middel, A., Wagner, M., Hoots, D., Smith, M., Brazel, A., 2020. Validation of seasonal mean radiant temperature simulations in hot arid urban climates. Sci. Total Environ. 749, 141392. https://doi.org/10.1016/j.scitotenv.2020.141392.

de Freitas, C.R., Grigorieva, E.A., 2017. A comparison and appraisal of a comprehensive range of human thermal climate indices. Int. J. Biometeorol. 61, 487–512. https://doi.org/10.1007/s00484-016-1228-6.

Delgado-Enales, I., Lizundia-Loyola, J., Molina-Costa, P., Del Ser, J., 2025. A machine learning approach for the efficient estimation of ground-level air temperature in urban areas. Urban Clim. 61, 102415. https://doi.org/10.1016/j.uclim.2025.102415.

Di Napoli, C., Barnard, C., Prudhomme, C., Cloke, H.L., Pappenberger, F., 2021. ERA5-HEAT: a global gridded historical dataset of human thermal comfort indices from climate reanalysis. Geosci Data J 8, 2–10. https://doi.org/10.1002/gdj3.102.

Dodman, D., Hayward, B., Pelling, M., Castan Broto, V., Chow, W., Chu, E., Dawson, R., Khirfan, L., McPhearson, T., Prakash, A., Zheng, Y., Ziervogel, G., 2022. Cities, Settlements and Key Infrastructure. In: Pörtner, H.O., Roberts, D.C., Tignor, M., Poloczanska, E.S., Mintenbeck, K., Alegría, A., Craig, M., Langsdorf, S., Löschke, S., Möller, V., Okem, A., Rama, B. (Eds.), Climate Change 2022: Impacts, Adaptation and Vulnerability. Contribution of Working Group II to the Sixth Assessment Report of the Intergovernmental Panel on Climate Change. Cambridge University Press, Cambridge, UK and New York, USA, pp. 907–1040. https://doi.org/10.1017/9781009325844.008.907.

Dosovitskiy, A., Fischer, P., Ilg, E., Häusser, P., Hairbacs, C., Golkov, V.D., Smagt, P., Cremers, D., Brox, T., 2015. FlowNet: Learning Optical Flow with Convolutional Networks. In: IEEE International Conference on Computer Vision (ICCV).

DWD Climate Data Center (CDC), 2025. Vieljährige Stationsmittelwerte für die Klimareferenzperiode 1991–2020 accessed [13.05.2025] [WWW Document].

Epstein, Y., Moran, D.S., 2006. Thermal comfort and the heat stress indices. Ind. Health 44, 388–398. https://doi.org/10.2486/indhealth.44.388.

Fauzi, F., Kuswanto, H., Atok, R.M., 2020. Bias correction and statistical downscaling of earth system models using quantile delta mapping (QDM) and bias correction constructed analogues with quantile mapping reordering (BCCAQ). J. Phys. Conf. Ser. 1538, 12050. https://doi.org/10.1088/1742-6596/1538/1/012050.

Feigel, G., Plein, M., Zeeman, M., Metzger, S., Matzarakis, A., Schindler, D., Christen, A., 2025. High spatio-temporal and continuous monitoring of outdoor thermal comfort in urban areas: a generic and modular sensor network and outreach platform. Sustain. Cities Soc. 119, 105991. https://doi.org/10.1016/j.scs.2024.105991.

Fenner, D., Meier, F., Bechtel, B., Otto, M., Scherer, D., 2017. Intra and inter 'local climate zone' variability of air temperature as observed by crowdsourced citizen weather stations in Berlin, Germany. Meteorol. Z. 26, 525–547. https://doi.org/10.1127/metz/2017/0861.

Fiala, D., Lomas, K.J., Stohrer, M., 2001. Computer prediction of human thermoregulatory and temperature responses to a wide range of environmental conditions. Int. J. Biometeorol. 45, 143–159. https://doi.org/10.1007/s004840100099.

Fünfgeld, H., Christen, A., Briegel, F., Schrodi, S., Speidel, A., Felder, C., Hoffmann, J., Irscheid, L., Merkle, D., Meyer, J., Schindler, D., Wehrle, J., Zengerling, C., 2025. Optimizing urban greening and densification in the context of outdoor heat: opportunities for AI-supported urban adaptation. Landscape and Urban Planning. In Review.

Georgescu, M., Broadbent, A.M., Krayenhoff, E.S., 2023. Quantifying the decrease in heat exposure through adaptation and mitigation in twenty-first-century US cities. Nature Cities 1, 42–50. https://doi.org/10.1038/s44284-023-00001-9.

Giometto, M.G., Christen, A., Meneveau, C., Fang, J., Krafczyk, M., Parlange, M.B., 2016. Spatial characteristics of roughness sublayer mean flow and turbulence over a realistic urban surface. Bound.-Lay. Meteorol. 160, 425–452. https://doi.org/10.1007/s10546-016-0157-6.

Giometto, M.G., Christen, A., Egli, P.E., Schmid, M.F., Tooke, R.T., Coops, N.C., Parlange, M.B., 2017. Effects of trees on mean wind, turbulence and momentum exchange within and above a real urban environment. Adv. Water Resour. 106, 154–168. https://doi.org/10.1016/j.advwatres.2017.06.018.

Haberstroh, S., Werner, C., Grün, M., Kreuzwieser, J., Seifert, T., Schindler, D., Christen, A., 2022. Central European 2018 hot drought shifts scots pine forest to its tipping point. Plant Biol. 24, 1186–1197. https://doi.org/10.1111/plb.13455.

Hastie, T., Tibshirani, R., Friedman, J., 2009. The Elements of Statistical Learning, Springer Series in Statistics. Springer, New York, NY, USA.

Hundhausen, M., Feldmann, H., Laube, N., Pinto, J.G., 2023. Future heat extremes and impacts in a convection-permitting climate ensemble over Germany. Nat. Hazards Earth Syst. Sci. 23, 2873–2893. https://doi.org/10.5194/nhess-23-2873-2023.

Järvi, L., Grimmond, C.S.B., Christen, A., 2011. The surface urban energy and water balance scheme (SUEWS): evaluation in Los Angeles and Vancouver. J Hydrol (Amst) 411, 219–237. https://doi.org/10.1016/j.jhydrol.2011.10.001.

Krayenhoff, E.S., Moustaoui, M., Broadbent, A.M., Gupta, V., Georgescu, M., 2018. Diurnal interaction between urban expansion, climate change and adaptation in US cities. Nat Clim Chang 8, 1097–1103. https://doi.org/10.1038/s41558-018-0320-9.

Krayenhoff, E.S., Broadbent, A.M., Zhao, L., Georgescu, M., Middel, A., Voogt, J.A., Martilli, A., Sailor, D.J., Erell, E., 2021. Cooling hot cities: a systematic and critical review of the numerical modelling literature. Environ. Res. Lett. 16, 53007. https://doi.org/10.1088/1748-9326/abdcf1.

Lamberti, G., Della Vista, D., Leccese, F., Salvadori, G., 2025. A novel methodology for evaluating urban surface overheating and its impact on pedestrians' radiative heat exposure using infrared thermography. Build. Environ. 278, 112981. https://doi.org/10.1016/j.buildenv.2025.112981.

Lindberg, F., Holmer, B., Thorsson, S., 2008. SOLWEIG 1.0 – modelling spatial variations of 3D radiant fluxes and mean radiant temperature in complex urban settings. Int. J. Biometeorol. 52, 697–713. https://doi.org/10.1007/s00484-008-0162-7.

Lindberg, F., Thorsson, S., Rayner, D., Lau, K., 2016. The impact of urban planning strategies on heat stress in a climate-change perspective. Sustain. Cities Soc. 25, 1–12. https://doi.org/10.1016/j.scs.2016.04.004.

Lindberg, F., Grimmond, C.S.B., Gabey, A., Huang, B., Kent, C.W., Sun, T., Theeuwes, N.E., Järvi, L., Ward, H.C., Capel-Timms, I., Chang, Y., Jonsson, P., Krave, N., Liu, D., Meyer, D., Olofson, K.F.G., Tan, J., Wästberg, D., Xue, L., Zhang, Z., 2018. Urban multi-scale environmental predictor (UMEP): an integrated tool for city-based climate services. Environ. Model. Software 99, 70–87. https://doi.org/10.1016/j.envsoft.2017.09.020.

Lu, J., Li, W., Hobeichi, S., Azad, S.A., Nazarian, N., 2025. Machine learning predicts pedestrian wind flow from urban morphology and prevailing wind direction. Environ. Res. Lett. 20, 054006. https://doi.org/10.1088/1748-9326/adc148.

Luo, T., Chen, M., 2025. Advancements in supervised machine learning for outdoor thermal comfort: a comprehensive systematic review of scales, applications, and data types. Energ. Buildings 329, 115255. https://doi.org/10.1016/j.enbuild.2024.115255.

Masson, V., Lemonsu, A., Hidalgo, J., Voogt, J., 2020. Urban climates and climate change. Annu. Rev. Env. Resour. 45, 411–444. https://doi.org/10.1146/annurev-environ-012320-083623.

Meili, N., Acero, J.A., Peleg, N., Manoli, G., Burlando, P., Fatichi, S., 2021. Vegetation cover and plant-trait effects on outdoor thermal comfort in a tropical city. Build. Environ. 195, 107733. https://doi.org/10.1016/j.buildenv.2021.107733.

Middel, A., Selover, N., Hagen, B., Chhetri, N., 2016. Impact of shade on outdoor thermal comfort—a seasonal field study in Tempe, Arizona. Int. J. Biometeorol. 60, 1849–1861. https://doi.org/10.1007/s00484-016-1172-5.

Middel, A., AlKhaled, S., Schneider, F.A., Hagen, B., Coseo, P., 2021. 50 grades of shade. Bull. Am. Meteorol. Soc. 102, E1805–E1820. https://doi.org/10.1175/BAMS-D-20-0193.1.

Mora, C., Dousset, B., Caldwell, I.R., Powell, F.E., Geronimo, R.C., Bielecki, C.R., Counsell, C.W.W., Dietrich, B.S., Johnston, E.T., Louis, L.V., Lucas, M.P., McKenzie, M.M., Shea, A.G., Tseng, H., Giambelluca, T.W., Leon, L.R., Hawkins, E., Trauernicht, C., 2017. Global risk of deadly heat. Nat. Clim. Chang. 7, 501–506. https://doi.org/10.1038/nclimate3322.

Muñoz Sabater, J., 2019. ERA5-land hourly data from 1981 to present. Copernicus climate change service (C3S) climate data store (CDS). (accessed on < 21-11-2024 >) [WWW document]. https://doi.org/10.24381/cds.e2161bac.

Muñoz Sabater, J., 2021. ERA5-land hourly data from 1950 to 1980. Copernicus climate change service (C3S) climate data store (CDS) (accessed on < 21-11-2024 >). https://doi.org/10.24381/cds.e2161bac.

Nam, C., Lierhammer, L., Buntemeyer, L., Evadzi, P., Cabana, D., Celliers, L., 2024. Changes in universal thermal climate index from regional climate model projections over European beaches. Clim Serv 34, 100447. https://doi.org/10.1016/j.cliser.2024.100447.

Nice, K.A., Nazarian, N., Lipson, M.J., Hart, M.A., Seneviratne, S., Thompson, J., Naserikia, M., Godic, B., Stevenson, M., 2022. Isolating the impacts of urban form and fabric from geography on urban heat and human thermal comfort. Build. Environ. 224, 109502. https://doi.org/10.1016/j.buildenv.2022.109502.

Oke, T.R., 1982. The energetic basis of the urban heat island. Q. J. Roy. Meteorol. Soc. 108, 1–24. https://doi.org/10.1002/qj.49710845502.

Oke, T.R., Mills, G., Christen, A., Voogt, J.A., 2017. Urban Climates. Cambridge University Press. https://doi.org/10.1017/9781139016476.
Paranunzio, R., Dwyer, E., Fitton, J.M., Alexander, P.J., O'Dwyer, B., 2021. Assessing current and future heat risk in Dublin city. Ireland. Urban Clim 40, 100983. https://doi.org/10.1016/j.uclim.2021.100983.
Parsons, K., 2002. Human thermal environments: the effects of hot, moderate, and cold environments on human health, comfort, and performance, Third edition. CRC Press. https://doi.org/10.1201/b16750.
Paszke, A., Gross, S., Massa, F., Lerer, A., Bradbury, J., Chanan, G., Killeen, T., Lin, Z., Gimelshein, N., Antiga, L., Desmaison, A., Kopf, A., Yang, E., DeVito, Z., Raison, M., Tejani, A., Chilamkurthy, S., Steiner, B., Fang, L., Bai, J., Chintala, S., 2019. PyTorch: An imperative style, high-performance deep learning library. In: Wallach, H., Larochelle, H., Beygelzimer, A., Alché-Buc, F., Fox, E., Garnett, R. (Eds.), Advances in Neural Information Processing Systems 32. Curran Associates, Inc, pp. 8024–8035. https://doi.org/10.48550/arXiv.1912.01703.
Perkins-Kirkpatrick, S.E., Lewis, S.C., 2020. Increasing trends in regional heatwaves. Nat. Commun. 11, 3357. https://doi.org/10.1038/s41467-020-16970-7.
Plein, M., Kersten, F., Zeeman, M., Christen, A., 2024. Street-level weather station network in Freiburg, Germany: station documentation (1.0). Zenodo. https://doi.org/10.5281/zenodo.12732552.
Qian, W., Chang, H.H., 2021. Projecting health impacts of future temperature: a comparison of quantile-mapping Bias-correction methods. Int. J. Environ. Res. Public Health 18. https://doi.org/10.3390/ijerph18041992.
Ronneberger, O., Fischer, P., Brox, T., 2015. In: Navab, N., Hornegger, J., Wells, W.M., Frangi, A.F. (Eds.), U-Net: Convolutional Networks for Biomedical Image Segmentation BT - Medical Image Computing and Computer-Assisted Intervention – MICCAI 2015. Springer International Publishing, Cham, pp. 234–241. https://doi.org/10.48550/arXiv.1505.04597.
Schiefer, F., Schmidtlein, S., Hartmann, H., Schnabel, F., Kattenborn, T., 2024. Large-scale remote sensing reveals that tree mortality in Germany appears to be greater than previously expected. Forestry: An International Journal of Forest Research. https://doi.org/10.1093/forestry/cpae062.
Schrodi, S., Briegel, F., Argus, M., Christen, A., Brox, T.. Climate-Sensitive Urban Planning through Optimization of Tree Placements. https://doi.org/10.48550/arXiv.2310.05691.
Seneviratne, S.I., Zhang, X., Adnan, M., Badi, W., Dereczynski, C., Di Luca, A., Ghosh, S., Iskandar, I., Kossin, J., Lewis, S., Otto, F., Pinto, I., Satoh, M., Vicente-Serrano, S.M., Wehner, M., Zhou, B., 2021. Weather and climate extreme events in a changing climate. In: Masson-Delmotte, V., Zhai, P., Pirani, A., Connors, S.L., Péan, C., Berger, S., Caud, N., Chen, Y., Goldfarb, L., Gomis, M.I., Huang, M., Leitzell, K., Lonnoy, E., Matthews, J.B.R., Maycock, T.K., Waterfield, T., Yelekçi, O., Yu, R., Zhou, B. (Eds.), Climate Change 2021: The Physical Science Basis. Contribution of Working Group I to the Sixth Assessment Report of the Intergovernmental Panel on Climate Change. Cambridge University Press, Cambridge, United Kingdom and New York, NY, USA, pp. 1513–1766. https://doi.org/10.1017/9781009157896.013.
Stewart, I.D., Oke, T.R., 2012. Local climate zones for urban temperature studies. Bull. Am. Meteorol. Soc. 93, 1879–1900. https://doi.org/10.1175/BAMS-D-11-00019.1.
Stone, B., Mallen, E., Rajput, M., Gronlund, C.J., Broadbent, A.M., Krayenhoff, E.S., Augenbroe, G., O'Neill, M.S., Georgescu, M., 2021. Compound climate and infrastructure events: how electrical grid failure alters heat wave risk. Environ. Sci. Technol. 55, 6957–6964. https://doi.org/10.1021/acs.est.1c00024.
Sulzer, M., Christen, A., 2024. Climate projections of human thermal comfort for indoor workplaces. Clim. Change 177, 28. https://doi.org/10.1007/s10584-024-03685-7.
Thorsson, S., Rayner, D., Lindberg, F., Monteiro, A., Katzschner, L., Lau, K.K.-L., Campe, S., Katzschner, A., Konarska, J., Onomura, S., Velho, S., Holmer, B., 2017. Present and projected future mean radiant temperature for three European cities. Int. J. Biometeorol. 61, 1531–1543. https://doi.org/10.1007/s00484-017-1332-2.
Unger, J., Skarbit, N., Kovács, A., Gál, T., 2020. Comparison of regional and urban outdoor thermal stress conditions in heatwave and normal summer periods: a case study. Urban Clim. 32, 100619. https://doi.org/10.1016/j.uclim.2020.100619.
United Nations, Department of Economic and Social Affairs, Population Division, 2019. World Urbanization Prospects: The 2018 Revision (ST/ESA/SER.A/420). United Nations, New York.
van Vuuren, D.P., Edmonds, J., Kainuma, M., Riahi, K., Thomson, A., Hibbard, K., Hurtt, G.C., Kram, T., Krey, V., Lamarque, J.-F., Masui, T., Meinshausen, M., Nakicenovic, N., Smith, S.J., Rose, S.K., 2011. The representative concentration pathways: an overview. Clim. Change 109, 5. https://doi.org/10.1007/s10584-011-0148-z.
Wallenberg, N., Rayner, D., Lindberg, F., Thorsson, S., 2023. Present and future heat stress of preschoolers in five Swedish cities. Clim. Risk Manag. 40, 100508. https://doi.org/10.1016/j.crm.2023.100508.
Wang, J., Chen, Y., Liao, W., He, G., Tett, S.F.B., Yan, Z., Zhai, P., Feng, J., Ma, W., Huang, C., Hu, Y., 2021. Anthropogenic emissions and urbanization increase risk of compound hot extremes in cities. Nat Clim Chang 11, 1084–1089. https://doi.org/10.1038/s41558-021-01196-2.
Ward, H.C., Kotthaus, S., Järvi, L., Grimmond, C.S.B., 2016a. Surface urban energy and water balance scheme (SUEWS): development and evaluation at two UK sites. Urban Clim. 18, 1–32. https://doi.org/10.1016/j.uclim.2016.05.001.
Ward, K., Lauf, S., Kleinschmit, B., Endlicher, W., 2016b. Heat waves and urban heat islands in Europe: a review of relevant drivers. Sci. Total Environ. 569–570, 527–539. https://doi.org/10.1016/j.scitotenv.2016.06.119.
Weeding, B., Love, P., Beyer, K., Lucieer, A., Remenyi, T., 2024. High-resolution projections of outdoor thermal stress in the twenty-first century: a Tasmanian case study. Int. J. Biometeorol. https://doi.org/10.1007/s00484-024-02622-8.
Wehrle, J., Jung, C., Giometto, M., Christen, A., Schindler, D., 2024. Introducing new morphometric parameters to improve urban canopy air flow modeling: a CFD to machine-learning study in real urban environments. Urban Clim. 58, 102173. https://doi.org/10.1016/j.uclim.2024.102173.
Yang, M., Ren, C., Wang, H., Wang, J., Feng, Z., Kumar, P., Haghighat, F., Cao, S.-J., 2024. Mitigating urban heat island through neighboring rural land cover. Nature Cities 1, 522–532. https://doi.org/10.1038/s44284-024-00091-z.
Zeeman, M., Christen, A., Grimmond, S., Fenner, D., Morrison, W., Feigel, G., Sulzer, M., Chrysoulakis, N., 2024. Modular approach to near-time data management for multi-city atmospheric environmental observation campaigns. Geoscientific Instrumentation, Methods and Data Systems 13, 393–424. https://doi.org/10.5194/gi-13-393-2024.
Zhao, L., Oleson, K., Bou-Zeid, E., Krayenhoff, E.S., Bray, A., Zhu, Q., Zheng, Z., Chen, C., Oppenheimer, M., 2021. Global multi-model projections of local urban climates. Nat Clim Chang 11, 152–157. https://doi.org/10.1038/s41558-020-00958-8.